Physica D 351–352 (2017) 1–13

Contents lists available at ScienceDirect

Physica D

journal homepage: www.elsevier.com/locate/physd

Solution landscapes in nematic microfluidics

M. Crespo [a,*], A. Majumdar [b], A.M. Ramos [c], I.M. Griffiths [d]

[a] UMR MISTEA - Mathématiques, Informatique et Statistique pour l´ Environnement et l´Agronomie (INRA/SupAgro). 2, Place P.Viala, 34060 Montpellier, France

[b] Department of Mathematical Sciences, University of Bath, Bath, BA2 7AY, UK

[c] Departamento de Matemática Aplicada & Instituto de Matemática Interisciplinar, Universidad Complutense de Madrid, Plaza de Ciencias, 3, 28040 Madrid, Spain

[d] Mathematical Institute, Radcliffe Observatory Quarter, University of Oxford, Oxford, OX2 6GG, UK

HIGHLIGHTS

- We explore the equilibria in nematic microfluidics as a function of pa- rameters ($\mathcal{G}$, $\mathcal{B}$).
- We demonstrate multistability for admissible pairs ($\mathcal{G}$, $\mathcal{B}$).
- We perform an asymptotic analysis of the static equilibria in the limits $\mathcal{G} \to 0$ and $\mathcal{G} \to \infty$.
- We study the sensitivity of the dynamic solutions to initial conditions.
- We control the final steady state by manipulating the rate of change of $\mathcal{G}$ and $\mathcal{B}$.

ARTICLE INFO

Article history:
Received 21 July 2016
Received in revised form
21 April 2017
Accepted 25 April 2017
Available online 4 May 2017
Communicated by C. Josserand

Keywords:
Leslie–Ericksen model
Nematic microfluidics
Asymptotic analysis
Anchoring strength

ABSTRACT

We study the static equilibria of a simplified Leslie–Ericksen model for a unidirectional uniaxial nematic flow in a prototype microfluidic channel, as a function of the pressure gradient $\mathcal{G}$ and inverse anchoring strength, $\mathcal{B}$. We numerically find multiple static equilibria for admissible pairs ($\mathcal{G}$, $\mathcal{B}$) and classify them according to their winding numbers and stability. The case $\mathcal{G} = 0$ is analytically tractable and we numerically study how the solution landscape is transformed as $\mathcal{G}$ increases. We study the one-dimensional dynamical model, the sensitivity of the dynamic solutions to initial conditions and the rate of change of $\mathcal{G}$ and $\mathcal{B}$. We provide a physically interesting example of how the time delay between the applications of $\mathcal{G}$ and $\mathcal{B}$ can determine the selection of the final steady state.

1. Introduction

Recent years have seen a tremendous surge in research in complex fluids, of which nematic liquid crystals (NLC) are a prime example [1–3]. Nematic liquid crystals are anisotropic liquids that combine the fluidity of liquids with the orientational order of solids i.e. the constituent rod-like molecules typically align along certain preferred or distinguished directions and this orientational anisotropy can have a profound optical signature [4]. Various researchers have already looked at effects of magnetic, electric or flow fields on pattern formation in confined nematic systems [1,5]. In particular, microfluidics is a thriving area of research; scientists typically manipulate fluid flow, say conventional isotropic fluids, in narrow channels complemented by different boundary treatments, leading to novel transport and mixing phenomena for fluids and potentially new health and pharmaceutical applications [6–8]. A natural question to ask is what happens when we replace a conventional isotropic liquid with an anisotropic liquid, such as a nematic liquid crystal? [3] Nematic microfluidics have recently generated substantial interest by virtue of their optical, rheological and backflow properties along with their defect profiles [9].

In Sengupta et al. [3], the authors investigate, both experimentally and numerically, microfluidic channels filled with nematic solvents. The authors work with a thin microfluidic channel with length much greater than width and width much greater than depth. A crucial consideration is the choice of boundary conditions and the authors work with homeotropic or normal boundary conditions on the top and bottom channel surfaces, which

* Corresponding author.
E-mail addresses: maria.crespo-moya@umontpellier.fr (M. Crespo), a.majumdar@bath.ac.uk (A. Majumdar), angel@mat.ucm.es (A.M. Ramos), ian.griffiths@maths.ox.ac.uk (I.M. Griffiths).

http://dx.doi.org/10.1016/j.physd.2017.04.004
0167-2789/

require the molecules to be oriented in the direction of the surface normal. The anchoring strength is a measure of how strongly the boundary conditions are enforced: strong anchoring roughly corresponds to Dirichlet conditions for the director field and zero anchoring describes free (Neumann homogeneous) boundary conditions. We expect most experiments to have moderate to strong anchoring conditions. The authors impose a flow field transverse to the anchoring conditions so that there are at least two competing effects in the experiment: anchoring normal to the boundaries and flow along the length of the microfluidic channel. They work with weak, medium, and strong flow speeds in qualitative terms and observe complex flow transitions. In the weak-flow regime, the molecules are only weakly affected by the flow and the molecular orientations are largely determined by the anchoring conditions. As the flow strength increases, a complex coupling between the molecular alignments and the flow field emerges and the nematic molecules reorient to align somewhat with the flow field. The medium-flow director field exhibits boundary layers near the center and the boundaries where the director field is strongly influenced by either the flow field or the boundary conditions. In the strong-flow regime, the molecules are almost entirely oriented with the flow field, with the exception of thin boundary layers near the channel surfaces to match the boundary conditions. The authors study these transitions experimentally and their experimental results suggest a largely *uniaxial* profile wherein the molecules exhibit a single distinguished direction of molecular alignment and this direction is referred to as being the *director* in the literature [1]. The authors present experimental measurements for the optical profiles and flow fields and their experimental work is complemented by a numerical analysis of the nematodynamic equations in the Beris–Edwards theory [10]. The Beris–Edwards theory is one of the most general formulations of nematodynamics, that accounts for both uniaxial and biaxial systems (with a primary and secondary direction of molecular alignment) and variations in the degree of orientational order. The authors numerically reproduce the experimentally observed flow transitions, the director and flow-field profiles, all of which are in good qualitative agreement with the experiments.

In Anderson et al. [11], the authors model this experimental set-up within the Leslie–Ericksen model for nematodynamics. Their Leslie–Ericksen model is restricted to uniaxial nematics with constant ordering (a constant degree of orientational order) [5]. They present governing equations for the flow field and the nematic director field along with the constitutive relations that describe the coupling between the director and the flow field (see Appendix A for details) and assume that all dependent variables only vary along the channel depth, with a unidirectional flow along the channel length, consistent with the experiments. These assumptions greatly simplify the mathematical model, yielding a decoupled system of partial differential equations for the director field, which captures the flow dynamics through a single variable: the pressure gradient, $\mathcal{G}$, along the channel length. The authors define two separate boundary-value problems: one for weak-flow solutions and one for strong-flow solutions, described by two different sets of boundary conditions for the director field. They find weak- and strong-flow solutions for all values of the pressure gradient and they relate the resulting flow profile to the mean flow speed by a standard Poiseuille-flow-type relation. The energy of the weak-flow solution is lower than the strong-flow solution for small $\mathcal{G}$ and there is an energy cross-over at some critical value, $\mathcal{G}^*$, that depends on the anchoring strength at the channel surfaces. Recently, Batista et al. [12] undertook a comprehensive study of the interplay between the pressure gradient and anchoring conditions on the transition between the weak-flow and strong-flow solutions, which they related to a discontinuity in the mass flow rate function.

In this paper, we build on the work in Anderson et al. [11] by performing an extensive study of the static solution landscape, complemented by some numerical investigations of the dynamical behavior, as the system evolves to these equilibrium configurations. We adopt the same model with the same underpinning assumptions as in Anderson et al. [11], but we do not define two separate boundary-value problems. We impose weak anchoring conditions for the director field on the top and the bottom surfaces since it includes both the weak and strong anchoring configurations and allows us to capture the competition between the flow field and the anchoring strength. In Bevilacqua et al. [13], the authors adopt a similar approach to study the competition between the magnetic field and the anchoring strength on static equilibrium profiles, described by critical points of a suitably defined energy.

We compute the static equilibrium solutions, using a combination of analytic and numerical methods, as a function of $\mathcal{G}$ and the inverse anchoring strength $\mathcal{B}$. The case $\mathcal{G} = 0$ is analytically tractable and we identify two different classes of solutions and characterize their stability. This is complemented by an asymptotic analysis in the limits $\mathcal{G} \to 0$ and $\mathcal{G} \to \infty$, with the latter regime yielding useful information about the boundary layers near channel surfaces, which are experimentally observed in the strong-flow regimes [3]. We then study the solution landscape for $\mathcal{G} \neq 0$ and track the stable and unstable solution branches as a function of $(\mathcal{G}, \mathcal{B})$. Our work largely focuses on the static equilibria but the last section is devoted to a numerical study of the dynamic Leslie–Ericksen model and its sensitivity to the initial condition. In particular, we present a numerical example for which we can control the final steady state by manipulating the rate of change of the pressure gradient and anchoring conditions.

The paper is organized as follows. In Section 2, we present the Leslie–Ericksen dynamic model, the governing equations and boundary conditions. In Section 3, we explore the static solution landscape as a function of the pressure gradient and anchoring strength. In Section 4, we study the dynamic model, with focus on the effects of initial conditions and the time-dependent forms of the pressure gradient and anchoring strength, and conclude in Section 5 by putting our work in context and discuss future developments.

2. Mathematical model

As in Anderson et al. [11], we model the NLC within the microfluidic channel in the Leslie–Ericksen framework. The channel has dimensions, $L_{\hat{x}} \gg L_{\hat{y}} \gg L_{\hat{z}}$, in the $\hat{x}$, $\hat{y}$ and $\hat{z}$ directions respectively, consistent with the experimental set-up in Anderson et al. [11] and Sengupta et al. [3] The NLC is purely uniaxial with constant order parameter, by assumption, and is hence fully described by a director field, $\boldsymbol{n}$, that represents the single preferred direction of nematic alignment. Here, $\boldsymbol{n}$ and $-\boldsymbol{n}$ are physically indistinguishable (in the absence of polarity the sign of $\boldsymbol{n}$ has no physical meaning). We additionally assume that all dependent variables only depend on the $\hat{z}$-coordinate, along the channel depth, as depicted in Fig. 1. Then the director field is of the form $\boldsymbol{n} = (\sin(\theta(\hat{z}, \hat{t})), 0, \cos(\theta(\hat{z}, \hat{t})))$ and the velocity field is unidirectional, of the form $\boldsymbol{v} = (\hat{u}(\hat{z}, \hat{t}), 0, 0)$, with $-h \leq \hat{z} \leq h$. Since $\boldsymbol{n}$ and $-\boldsymbol{n}$ are indistinguishable, θ and $\theta + k\pi$, $k \in \mathbb{Z}$, describe the same director profile. We assume that $\hat{u}(\hat{z}, \hat{t})$ is symmetric around the center-line (i.e. around $\hat{z} = 0$) and no-slip conditions are imposed on the channel walls (i.e. $\hat{u}(\pm h, \hat{t}) = 0$). We assume weak anchoring boundary conditions for θ on $\hat{z} = \pm h$, that can be derived from the well-known Rapini–Papoular weak-anchoring energy [14],

$$E_S = \int_{\hat{z}=\pm h} \frac{A}{2} \sin^2 \theta \, d\hat{x} \, d\hat{y},$$

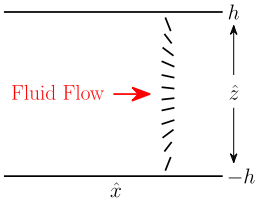

Fig. 1. Schematic of the microfluidic channel set-up. The nematic molecules are anchored at the top and bottom surfaces and are deformed by the fluid flow from the left.

which enforces $\theta(-h) = k_1\pi$ and $\theta(h) = k_2\pi$ ($k_1, k_2 \in \mathbb{Z}$) for large anchoring coefficients $A > 0$. In other words, the Rapini–Papoular energy enforces homeotropic anchoring (along the normal to the surface) described by, $\boldsymbol{n} = \pm(0, 0, 1)$ on $\hat{z} = \pm h$.

We substitute the assumed forms for $\boldsymbol{v}$ and $\boldsymbol{n}$into the full Leslie–Ericksen governing equations, as outlined in Appendix A, and obtain the following system describing the evolution of θ and $\hat{u}$:

$$\gamma_1 \frac{\partial\theta}{\partial\hat{t}} = K\frac{\partial^2\theta}{\partial\hat{z}^2} - \frac{\partial\hat{u}}{\partial\hat{z}}m(\theta) \qquad \hat{z}\in(-h,h),\ \hat{t}>0, \tag{1a}$$

$$-G\hat{z} = \frac{\partial\hat{u}}{\partial\hat{z}}g(\theta) + \frac{\partial\theta}{\partial\hat{t}}m(\theta) \qquad \hat{z}\in(-h,h),\ \hat{t}>0, \tag{1b}$$

$$\theta(\hat{z},0) = \Theta(\hat{z}) \qquad \hat{z}\in(-h,h), \tag{1c}$$

$$\hat{u}(\pm h,\hat{t}) = 0 \qquad \hat{t}>0, \tag{1d}$$

$$K\frac{\partial\theta}{\partial\hat{z}} = -\frac{A}{2}\sin(2\theta(\hat{z},\hat{t})) \qquad \hat{z}=h,\quad \hat{t}>0, \tag{1e}$$

$$K\frac{\partial\theta}{\partial\hat{z}} = \frac{A}{2}\sin(2\theta(\hat{z},\hat{t})) \qquad \hat{z}=-h,\quad \hat{t}>0, \tag{1f}$$

where K (N) is the elastic constant of the NLC, Θ is the initial condition, $-G = \frac{\partial P}{\partial\hat{x}}$ is the component of the pressure gradient in the channel direction and A (Nm^{-1}) is the surface anchoring strength. Note that for a physically realistic solution, we expect that as $A\to\infty$, 2θ tends to an integer multiple of π on $\hat{z} = \pm h$.

The functions

$$\hat{m}(\theta) = \hat{\alpha}_2\cos^2(\theta) - \hat{\alpha}_3\sin^2(\theta) \quad \text{and}$$

$$\hat{g}(\theta) = \hat{\alpha}_1\cos^2(\theta)\sin^2(\theta) + \frac{\hat{\alpha}_5-\hat{\alpha}_2}{2}\cos^2(\theta) + \frac{\hat{\alpha}_3+\hat{\alpha}_6}{2}\sin^2(\theta) + \frac{\hat{\alpha}_4}{2},$$

the $\hat{\alpha}_i$ (Nm^{-2} s), $i\in\{1,\dots,6\}$, are constant viscosities related to each other by the Parodi relation [15], $\hat{\alpha}_2+\hat{\alpha}_3 = \hat{\alpha}_6-\hat{\alpha}_5$. Characteristic values for the dimensionless nematic viscosities are $\alpha_1 = -0.1549$, $\alpha_2 = -0.9859$, $\alpha_3 = -0.0535$, $\alpha_5 = 0.7324$ and $\alpha_6 = -0.39$ [11]. Note that the following inequalities must be satisfied (see Appendix A.1.1):

$$\hat{g}(\theta) > 0, \qquad \hat{\gamma}_1\hat{g}(\theta) > \hat{m}^2(\theta), \tag{2}$$

where $\hat{\gamma}_1 = \hat{\alpha}_3 - \hat{\alpha}_2$.

We non-dimensionalize the system (1) using the scalings

$$z = \frac{\hat{z}}{h}, \qquad u = \frac{\hat{u}\alpha_4 h}{K}, \qquad \alpha_i = \frac{\hat{\alpha}_i}{\hat{\alpha}_4},$$

$$\gamma_1 = \frac{\hat{\gamma}_1}{\hat{\alpha}_4}, \qquad t = \frac{K\hat{t}}{\hat{\alpha}_4 h^2}. \tag{3}$$

Furthermore, using (1a), (1b) we obtain the following decoupled dimensionless initial–boundary-value problem for θ:

$$\big(\gamma_1 g(\theta) - m(\theta)^2\big)\frac{\partial\theta}{\partial t} = g(\theta)\frac{\partial^2\theta}{\partial z^2} + \mathcal{G}zm(\theta) \qquad z\in(-1,1),\ t>0, \tag{4a}$$

$$\theta(z,0) = \Theta(z) \qquad z\in(-1,1), \tag{4b}$$

$$\mathcal{B}\frac{\partial\theta}{\partial z}(1,t) = -\sin(2\theta(1,t)) \qquad t>0, \tag{4c}$$

$$\mathcal{B}\frac{\partial\theta}{\partial z}(-1,t) = \sin(2\theta(-1,t)) \qquad t>0, \tag{4d}$$

the velocity u being available via equation

$$u(z,t) = -\int \frac{\mathcal{G}z + \frac{\partial\theta}{\partial t}(z,t)m(\theta(z,t))}{g(\theta(z,t))}\mathrm{d}z, \tag{5}$$

where $\mathcal{G} = h^3G/K$ and $\mathcal{B} = 2K/Ah$ are the dimensionless pressure gradient and the dimensionless inverse anchoring strength respectively,

$$m(\theta) = \alpha_2\cos^2(\theta) - \alpha_3\sin^2(\theta) \quad \text{and}$$

$$g(\theta) = \alpha_1\cos^2(\theta)\sin^2(\theta) + \frac{1}{2}\big((\alpha_5-\alpha_2)\cos^2(\theta) + (\alpha_3+\alpha_6)\sin^2(\theta) + 1\big).$$

Note that, if θ_1, θ_2 are the solutions of (4) corresponding, respectively, to initial conditions $\Theta_1(z)$ and $\Theta_2(z) = \Theta_1(z) + k\pi$ ($k\in\mathbb{Z}$), then $\theta_2 = \theta_1 + k\pi$ and both θ_1 and θ_2 correspond to the same physical description.

We compute equilibrium solutions and dynamic time-dependent solutions of system (4) for different values of dimensionless pressure gradient $\mathcal{G}$, dimensionless inverse anchoring strength $\mathcal{B}$ and initial conditions Θ, using parameter values for the NLC 5CB as in Anderson et al. [11].

3. Equilibrium solutions

We begin by studying the static equilibria of the system (4), $\theta^*(z)$, which satisfy

$$\begin{cases} g(\theta^*(z))\dfrac{\mathrm{d}^2\theta^*}{\mathrm{d}z^2}(z) = -\mathcal{G}zm(\theta^*(z)) \quad z\in(-1,1), \\ \mathcal{B}\dfrac{\mathrm{d}\theta^*}{\mathrm{d}z}(1) = -\sin(2\theta^*(1)), \\ \mathcal{B}\dfrac{\mathrm{d}\theta^*}{\mathrm{d}z}(-1) = \sin(2\theta^*(-1)). \end{cases} \tag{6}$$

We characterize the equilibrium solutions in terms of their winding number, defined to be

$$\omega(\theta^*) = \frac{\theta^*(1)-\theta^*(-1)}{2\pi}. \tag{7}$$

The winding number is typically used in the literature in relation with topological defects [16], however here we use it as a measure of the rotation of the director field between the top and bottom surfaces. The limit $\mathcal{B}\to 0$ is the strong anchoring limit, when the boundary conditions on $z = \pm1$ are strongly enforced and both $\theta^*(1)$ and $\theta^*(-1)$ are integer multiples of $\frac{\pi}{2}$ in this limit. Particularly, as we will see in Section 3.1, as $\mathcal{B}\to 0$, the stable equilibria at $z = \pm1$ tend to $\theta^*(\pm1) = n\pi$, $n\in\mathbb{Z}$ (homeotropic anchoring) and the unstable equilibria to $\theta^*(\pm1) = (n+\frac{1}{2})\pi$, $n\in\mathbb{Z}$ (planar anchoring at the boundaries). This is simply because $\theta^*(\pm1) = n\pi$ is a minimum of the surface energy used to derive the anchoring conditions at $z = \pm1$. See Appendix B.1.1 for a detailed description of different nematic configurations. In what follows, we track the stable and unstable solutions of (6) as the model parameters are varied.

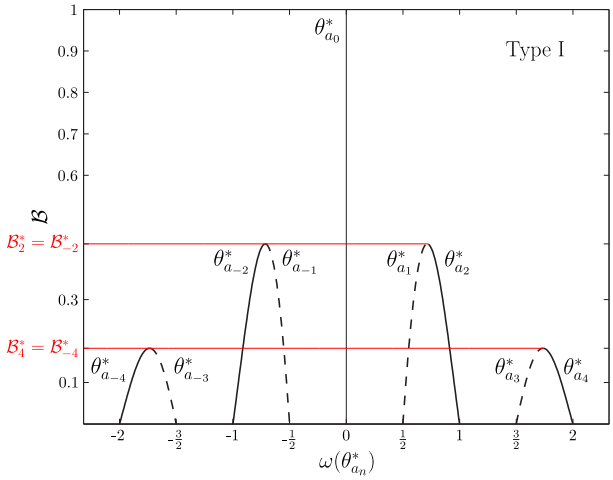

Fig. 2. Case $\mathcal{G} = 0$: Solutions of (10) indicating the emergence of non-constant steady-state solutions $\theta^*_{a_n}$, $n = 0, \pm1, \ldots$ at critical values $\mathcal{B}^*_{2n}$ for $n = \pm1, \pm2, \ldots$. The solid and dashed lines represent, respectively, the values of $\omega(\theta^*_{a_n})$ for which the steady state $\theta^*_{a_n}$ is stable or unstable.

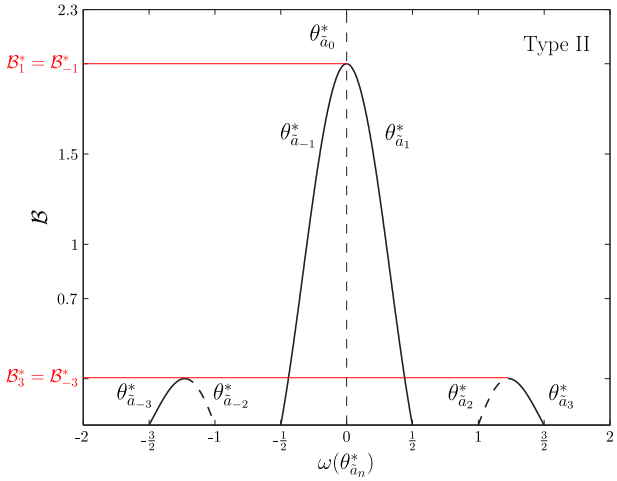

Fig. 3. Case $\mathcal{G} = 0$: Solutions of (11) indicating the emergence of non-constant steady-state solutions $\theta^*_{\tilde{a}_n}$, $n = 0, \pm1, \ldots$ at critical values $\mathcal{B}^*_{2n+1}$ for $n = 0, \pm1, \ldots$. The solid and dashed lines represent, respectively, the values of $\omega(\theta^*_{\tilde{a}_n})$ for which the steady state $\theta^*_{\tilde{a}_n}$ is stable or unstable.

3.1. No fluid flow ($\mathcal{G} = 0$)

When $\mathcal{G} = 0$, we can explicitly solve the system (6) to obtain the static equilibria (see Appendix B for more details). We divide the potentially stable equilibria (see Appendix B.1) into two families:

$$\text{Type I } \theta^*_{a_n}(z) = a_n z, \quad \text{where } \mathcal{B}a_n = -\sin(2a_n), \tag{8}$$

$$\text{Type II } \theta^*_{\tilde{a}_n}(z) = \tilde{a}_n z + \frac{\pi}{2}, \quad \text{where } \mathcal{B}\tilde{a}_n = \sin(2\tilde{a}_n). \tag{9}$$

For every value of $\mathcal{B}$, we obtain an ordered set of solutions for (8), with $0 = a_0 < a_1 < \cdots < a_n$, $n \in \mathbb{N} \cup \{0\}$ depending on $\mathcal{B}$. Moreover, if a_n defines a solution, so does $-a_n$, which we denote by a_{-n} (identical remarks apply to (9)). Let $\theta^*_{a_n}$ denote the solution corresponding to a_n in (8), then $\theta^*_{a_n} = -\theta^*_{a_{-n}}$ and $\omega(\theta^*_{a_n}) = -\omega(\theta^*_{a_{-n}}) = \frac{a_n}{\pi}$, where $\omega(\theta^*_{a_n})$ satisfies the transcendental equation

$$\mathcal{B} = -\frac{\sin(2\pi\omega(\theta^*_{a_n}))}{\pi\omega(\theta^*_{a_n})}. \tag{10}$$

Analogous statements apply to solutions $\theta^*_{\tilde{a}_n}$ with $\tilde{a}_n$ a solution of Eq. (9), where $\omega(\theta^*_{\tilde{a}_n})$ satisfies the transcendental equation

$$\mathcal{B} = \frac{\sin(2\pi\omega(\theta^*_{\tilde{a}_n}))}{\pi\omega(\theta^*_{\tilde{a}_n})}. \tag{11}$$

Thus there is a symmetric (with respect to $\omega(\theta^*) = 0$) arrangement of solutions, which is physically reasonable since we do not expect to have a preferred twist direction when $\mathcal{G} = 0$. In Appendix B.1 we analyze the linear stability of the equilibria (8)–(9) to conclude that

Type I is stable if n is even and is unstable if n is odd,
Type II is stable if n is odd and is unstable if n is even.

It is clear that the director profiles for $\theta^*_{a_n}$ and $\theta^*_{a_{-n}}$ are reflections of each other about the angle $\theta = 0$. The constant solutions $\theta^*_{a_0} \equiv 0$ and $\theta^*_{\tilde{a}_0} \equiv \frac{\pi}{2}$ exist for all values of $\mathcal{B}$. These are the only solutions for large values of $\mathcal{B}$. Non-constant solutions subject to (8) and (9) emerge as $\mathcal{B}$ decreases.

We define critical values $\mathcal{B}^*_{2n}$ with $n = \pm1, \pm2, \ldots$ such that, for $n > 0$, the solution branches, $\left(\omega(\theta^*_{a_{2n}}), \mathcal{B}\right)$ and $\left(\omega(\theta^*_{a_{2n-1}}), \mathcal{B}\right)$ (and $\left(\omega(\theta^*_{a_{2n+1}}), \mathcal{B}\right)$ if $n < 0$) coalesce at the critical value $\mathcal{B} = \mathcal{B}^*_{2n}$ and cease to exist for $\mathcal{B} > \mathcal{B}^*_{2n}$ (see Fig. 2). Similarly, we define the critical values $\mathcal{B}^*_{2n+1}$ with $n = 0, \pm1, \ldots$ as the coalescence points for solutions of Type II (see Fig. 3 for a complete description). Solutions with large winding numbers are only observable in the strong-anchoring limit. Notice that for $\mathcal{B} \to 0$ the stable equilibria are either $\theta^*_{a_n}$ with $\omega(\theta^*_{a_n}) = k\pi$ or $\theta^*_{\tilde{a}_n}$ with $\omega(\theta^*_{\tilde{a}_n}) = (k + \frac{1}{2})\pi$, $k \in \mathbb{Z}$, and in both cases $\theta^*(\pm1)$ tends to a multiple of π. We can apply the same reasoning to deduce that for $\mathcal{B} \to 0$, the unstable equilibria are such that $\theta^*(\pm1) \to (k+\frac{1}{2})\pi$, as previously claimed before Section 3.1. For weaker anchoring, the director profile has greater freedom to reorient at the boundaries and escape from the energetically expensive fixed rotation imposed by large winding numbers. For $\mathcal{G} = 0$, $\mathcal{B}^*_i = \mathcal{B}^*_{-i}$ ($i \in \mathbb{N}$). For $\mathcal{B} > \mathcal{B}^*_1$, $\theta^*_{a_0}$ and $\theta^*_{\tilde{a}_0}$ are the only constant steady states of system (6). For simplicity, in what follows we denote the equilibrium solutions as θ^*_a, where $\theta^*_a = \theta^*_{a_n}$ if it is of Type I and $\theta^*_a = \theta^*_{\tilde{a}_n}$ if it is of Type II.

3.2. Fluid flow ($\mathcal{G} > 0$)

Next, we study the static equilibria of the system (6) when we apply a pressure difference $\mathcal{G} > 0$ across the microfluidic channel, inducing a fluid flow. The solutions are computed numerically for all values of $\mathcal{G}$ using *Chebfun* via the method of continuation [17]. When the $\mathcal{G} = 0$ solution θ^*_a is taken as the initial condition (see Section 3.1), the corresponding solution with $\mathcal{G} > 0$ is denoted by $\theta^*_{a,\mathcal{G}}$. We numerically compute the stability of the equilibria with $\mathcal{G} > 0$ (using the function *eigs* of the MATLAB package *Chebfun*) and find that the stability properties of the $\mathcal{G} = 0$ equilibria propagate to the $\mathcal{G} > 0$ cases.

3.2.1. Asymptotics when $\mathcal{G} \ll 1$

When $\mathcal{G} \ll 1$, we can approximate $\theta^*_{a,\mathcal{G}}$ by the expansion $\theta^*_{a,\mathcal{G}}(z) = \theta^*_a(z) + \mathcal{G}\theta^{(1)}_{\mathcal{G}}(z) + \cdots$, where θ^*_a is the corresponding solution for $\mathcal{G} = 0$. It is straightforward to verify that $\theta^{(1)}_{\mathcal{G}}$ is a solution of

$$\begin{cases} \dfrac{d^2\theta^{(1)}_{\mathcal{G}}}{dz^2}(z) = zQ\left(\theta^*_a(z)\right) \quad z \in (-1, 1) \\ \mathcal{B}\dfrac{d\theta^{(1)}_{\mathcal{G}}}{dz}(1) = -2\theta^{(1)}_{\mathcal{G}}(1)\cos(2\theta^{*a}(1)), \\ \mathcal{B}\dfrac{d\theta^{(1)}_{\mathcal{G}}}{dz}(-1) = 2\theta^{(1)}_{\mathcal{G}}(-1)\cos(2\theta^{*a}(-1)), \end{cases} \tag{12}$$

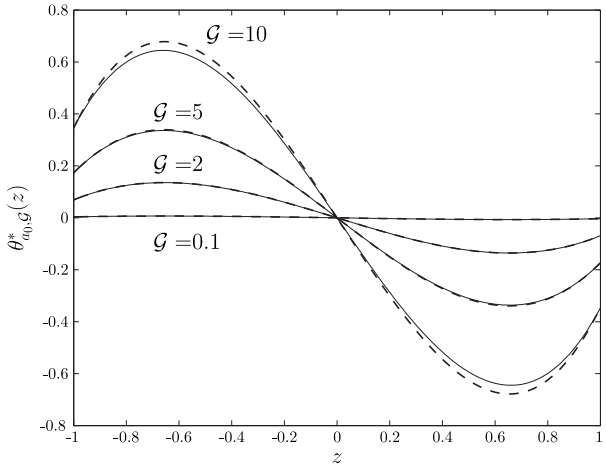

Fig. 4. Static equilibria $\theta^*_{a_0,\mathcal{G}}$ when $\mathcal{B} = \frac{1}{3}$. Comparison of the asymptotic solution given by (13) (dashed) with the full numerical solution to (6) (solid).

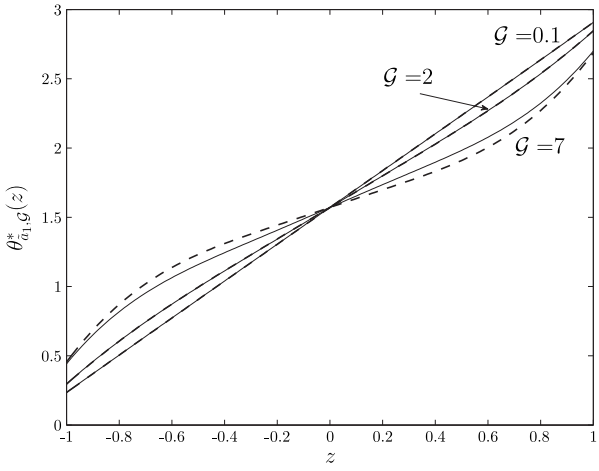

Fig. 5. Static equilibria $\theta^*_{\tilde{a}_1,\mathcal{G}}$ when $\mathcal{B} = \frac{1}{3}$. Comparison of the asymptotic solution given by (13) (dashed) with the full numerical solution to (6) (solid).

where $Q(s) = -m(s)/g(s)$. The solution to (12) is given by

$$\theta^{(1)}_{\mathcal{G}}(z) = J(z) + Cz + D, \tag{13}$$

where

$$I(r) = \int_0^r sQ(as+b)\mathrm{d}s, \qquad J(z) = \int_0^z I(r)\mathrm{d}r, \tag{14}$$

$$C = \frac{2(-1)^k \cos(2a)\big(J(-1) - J(1)\big) - \mathcal{B}\big(I(1) + I(-1)\big)}{2\mathcal{B} + 4(-1)^k \cos(2a)}, \tag{15}$$

$$D = -\frac{1}{2}\big(J(1) + J(-1)\big) + \frac{\mathcal{B}(-1)^k\big(I(-1) - I(1)\big)}{4\cos(2a)}, \tag{16}$$

with $b = k = 0$ for Type I solutions where a satisfies (8) and $b = \frac{\pi}{2}$ and $k = 1$ for Type II solutions, where a satisfies (9). We validate the asymptotic analysis performed above by numerically computing the equilibria $\theta^*_{a,\mathcal{G}}$ of (4) for small values of $\mathcal{G}$ by solving (6) with *Chebfun* and comparing this with the asymptotic result (13). When $\theta^*_a = \theta^*_{a_0} \equiv 0$ and $\theta^*_a = \theta^*_{\tilde{a}_1}$ the asymptotic solution approximates the actual solution for values of $\mathcal{G}$ significantly beyond the expected regime (see respectively Figs. 4(a) and 5(a), where we find that the asymptotic solution approximates the full numerical solution well for values of $\mathcal{G}$ as large as 7). We note that the graphical representation of the solutions $\theta^*_{a_0,\mathcal{G}}$ and $\theta^*_{\tilde{a}_1,\mathcal{G}}$ in Figs. 4 and 5 agrees well with the experimental situations reported by Jewell et al. [18], where the authors study the role of the pressure gradient into the transition between these two steady states in the limiting case $\mathcal{B} = 0$. We choose a moderate anchoring strength to illustrate the differences between the numerics and asymptotics clearly. The asymptotic approximations rapidly improve as $\mathcal{B} \to 0$. Fig. 6 plots the director field $\boldsymbol{n}$ and the flow profile u (obtained by using (5)) associated with the equilibria $\theta^*_{a_0,\mathcal{G}}$ and $\theta^*_{\tilde{a}_1,\mathcal{G}}$, computed when $\mathcal{G} = 0.5$ and $\mathcal{B} = \frac{1}{3}$. The director fields exhibit a continuous rotation between the two channel surfaces. This behavior is broadly known as the *tumbling regime* and is typically observed in nematic microfluidics with small flow rates [19]. We note that solutions $\theta^*_{a_0,\mathcal{G}}$ and $\theta^*_{\tilde{a}_1,\mathcal{G}}$ correspond to the weak- and strong-flow solutions (obtained with weak anchoring) in Anderson et al. [11], Fig. 6 being easily compared with Fig. 4(d)–(f) in [11]. In contrast to [11], our stability analysis suggests that both solutions are stable when $\mathcal{G} = 0.5$ and $\mathcal{B} = \frac{1}{3}$.

3.2.2. *Asymptotics when $\mathcal{G} \to \infty$*

For $\mathcal{G} \gg 1$, we can perform a similar asymptotic expansion of the form $\theta^*_{\mathcal{G}}(z) = \theta^{(0)}_{\mathcal{G}}(z) + (1/\mathcal{G})\theta^{(1)}_{\mathcal{G}}(z) + \cdots$. Substituting this expansion into (6) and equating terms at leading order gives

$$zQ(\theta^{(0)}_{\mathcal{G}}(z)) = 0, \quad z \in (-1, 1) \tag{17a}$$

$$\mathcal{B}\frac{\mathrm{d}\theta^{(0)}_{\mathcal{G}}}{\mathrm{d}z}(1) = -\sin(2\theta^{(0)}_{\mathcal{G}}(1)), \tag{17b}$$

$$\mathcal{B}\frac{\mathrm{d}\theta^{(0)}_{\mathcal{G}}}{\mathrm{d}z}(-1) = \sin(2\theta^{(0)}_{\mathcal{G}}(-1)). \tag{17c}$$

Eq. (17a) implies that $\theta^{(0)}_{\mathcal{G}}(0)$ can take arbitrary values in $\mathbb{R}$ and

$$\theta^{(0)}_{\mathcal{G}}(z) \equiv \pm\arctan\left(\sqrt{\frac{\alpha_2}{\alpha_3}}\right) + k\pi \equiv \sigma^{\pm}_k \tag{18}$$

with $k \in \mathbb{Z}$ arbitrary; the value σ^+_0 is broadly known as the *flow-aligning angle* or *Leslie angle* [20]. However, the boundary conditions (17b), (17c) are not satisfied by (18) and hence we expect to find boundary layers near $z = -1$, 0 and 1, in order to match the boundary conditions. The solution in the two outer regions $-1 < z < 0$ and $0 < z < 1$ are given by (18) for any two particular integer values of k, say k_1 and k_2.

Near $z = -1$, we rescale in (6) by introducing the variable $\eta = \sqrt{\mathcal{G}}(z+1)$ and perform an asymptotic expansion in powers of $1/\sqrt{\mathcal{G}}$. The corresponding leading-order term in $\mathcal{G}$, $\theta^{(0)}_{\mathrm{L},\mathcal{G}}(\eta)$, is a solution of

$$\frac{\mathrm{d}^2\theta^{(0)}_{\mathrm{L},\mathcal{G}}}{\mathrm{d}\eta^2}(\eta) = -Q(\theta^{(0)}_{\mathrm{L},\mathcal{G}}(\eta)), \quad \eta > 0 \tag{19a}$$

$$\bar{\mathcal{B}}\frac{\mathrm{d}\theta^{(0)}_{\mathrm{L},\mathcal{G}}}{\mathrm{d}\eta}(0) = \sin(2\theta^{(0)}_{\mathrm{L},\mathcal{G}}(0)), \tag{19b}$$

$$\lim_{\eta\to\infty}\theta^{(0)}_{\mathrm{L},\mathcal{G}}(\eta) = \sigma^{\pm}_{k_1}, \tag{19c}$$

where we have rescaled $\bar{\mathcal{B}} = \sqrt{\mathcal{G}}\mathcal{B}$ assuming that $\bar{\mathcal{B}} = O(1)$ to obtain the richest asymptotic limit. We point out that the asymptotic analysis could be done without this assumption. Then (19b) would be $\mathcal{B}\frac{\mathrm{d}\theta^{(0)}_{\mathrm{L},\mathcal{G}}}{\mathrm{d}\eta} = 0$ and $\theta^{(0)}_{\mathrm{L},\mathcal{G}}(\eta) = \sigma^{\pm}_{k_1}$. We would need to use the second term, $\theta^{(1)}_{\mathrm{L},\mathcal{G}}$, of the asymptotic expansion (at least) and the results with these two terms would be worse than those obtained here. Eq. (19c) is the matching condition between $\theta^{(0)}_{\mathrm{L},\mathcal{G}}$ and $\theta^{(0)}_{\mathcal{G}}$.

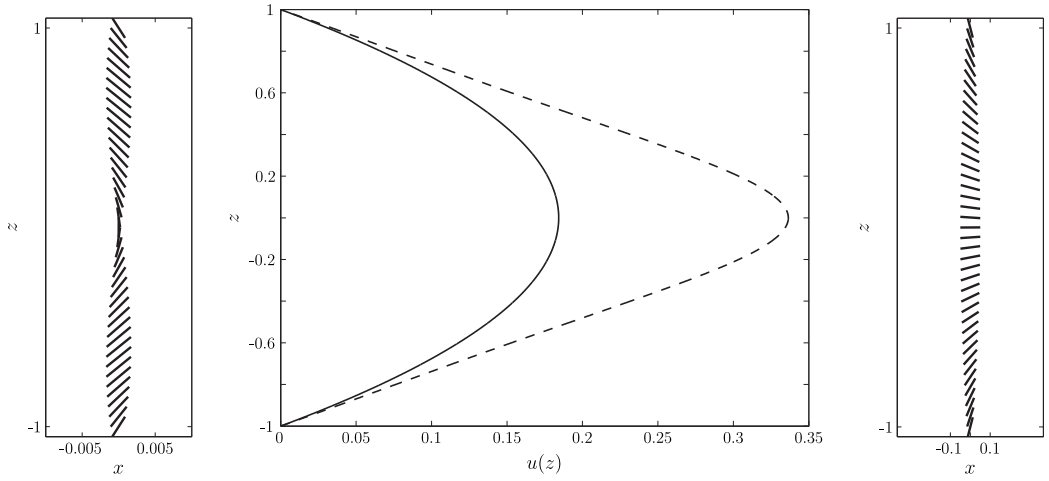

(a) $\boldsymbol{n}$ with $\theta^*_{a_0,0.5}$. (b) Velocity profiles associated to $\theta^*_{a_0,0.5}$ (solid) and $\theta^*_{a_1,0.5}$ (dashed). (c) $\boldsymbol{n}$ with $\theta^*_{a_1,0.5}$.

Fig. 6. Director and flow profiles associated with the static equilibria $\theta^*_{a_0,0.5}$ and $\theta^*_{a_1,0.5}$ when $\mathcal{B} = \frac{1}{3}$. We note that, in (a), $\boldsymbol{n} \approx (0, 0, 1)$ but different scales have been used in the x and z axis to allow the reader to appreciate the change between $\theta^*_{a_0,0.5}$ and $\theta^*_{a_0,0}$ (corresponding to $\boldsymbol{n} = (0, 0, 1)$). In (b), x and z axis have the same scale.

Near $z = 0$, we set $\xi = \mathcal{G}^{1/3} z$ and the corresponding leading-order term, $\theta^{(0)}_{\mathrm{C},\mathcal{G}}(\xi)$, satisfies

$$\frac{\mathrm{d}^2\theta^{(0)}_{\mathrm{C},\mathcal{G}}}{\mathrm{d}\xi^2} = \xi Q(\theta^{(0)}_{\mathrm{C},\mathcal{G}}(\xi)), \quad \xi \in (-\infty, \infty), \tag{20a}$$

$$\lim_{\xi\to-\infty} \theta^{(0)}_{\mathrm{C},\mathcal{G}}(\xi) = \sigma^{\pm}_{k_1}, \tag{20b}$$

$$\lim_{\xi\to\infty} \theta^{(0)}_{\mathrm{C},\mathcal{G}}(\eta) = \sigma^{\pm}_{k_2}, \tag{20c}$$

where (20b), (20c) describe the matching conditions.

Finally, we introduce the variable $\zeta = \sqrt{\mathcal{G}}(1 - z)$ near $z = 1$ and $\theta^{(0)}_{\mathrm{R},\mathcal{G}}(\zeta)$, the leading-order solution in $\mathcal{G}$, satisfies

$$\frac{\mathrm{d}^2\theta^{(0)}_{\mathrm{R},\mathcal{G}}}{\mathrm{d}\zeta^2} = Q(\theta^{(0)}_{\mathrm{R},\mathcal{G}}(\zeta)), \quad \zeta > 0, \tag{21a}$$

$$\bar{\mathcal{B}}\frac{\mathrm{d}\theta^{(0)}_{\mathrm{L},\mathcal{G}}}{\mathrm{d}\eta}(0) = \sin(2\theta^{(0)}_{\mathrm{L},\mathcal{G}}(0)), \tag{21b}$$

$$\lim_{\zeta\to\infty} \theta^{(0)}_{\mathrm{R},\mathcal{G}}(\zeta) = \sigma^{\pm}_{k_2}, \tag{21c}$$

where (21c) is the matching condition.

We numerically solve the three boundary layer problems (19)–(21), using *Chebfun*, matching to the constant values in (18). For our particular choice of dimensionless nematic viscosities α_2 and α_3, all values of $\sigma^{\pm}_k$ (defined in (18)) are close to some odd multiple of $\frac{\pi}{2}$, and thus the inner director field is largely flow-aligned and is rotated $k\pi$ times with respect to the flow direction. There are multiple choices for the outer solutions, $\sigma^{\pm}_{k_1}$ and $\sigma^{\pm}_{k_2}$, for $-1 < z < 0$ and $0 < z < 1$ respectively, yielding different asymptotic approximations. In Figs. 7 and 8 we compare the asymptotic approximations (18)–(21) with numerical solutions of the full system (6) for large values of $\mathcal{G}$. The two cases are labeled as $\theta^*_{a_0,\mathcal{G}}$ and $\theta^*_{a_1,\mathcal{G}}$ respectively, depending on the initial condition used to generate them. The values of $\sigma^{\pm}_{k_1}$ and $\sigma^{\pm}_{k_2}$ are extracted from the numerical solution and used in the asymptotic approximation (18)–(21) (these values are different for solutions $\theta^*_{a_0,\mathcal{G}}$ and $\theta^*_{a_1,\mathcal{G}}$). Once the outer values are determined, we can compute the asymptotic approximation using the methodology outlined above. The asymptotic solution approximates the full

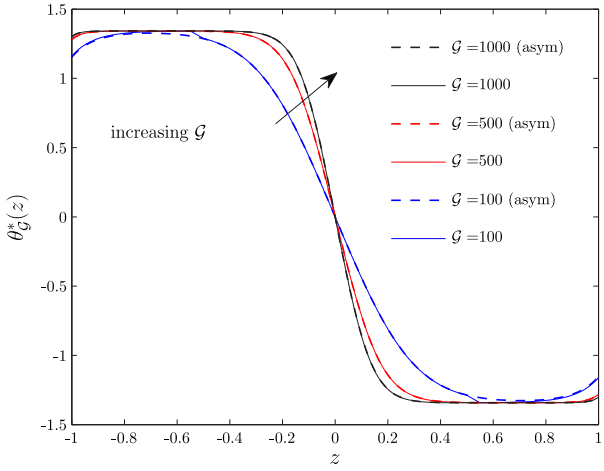

Fig. 7. Static equilibria $\theta^*_{a_0,\mathcal{G}}$ with $\mathcal{G} \to \infty$ and $\mathcal{B} = \frac{1}{3}$. Comparison of asymptotic solution given by (13) (dashed) with the full numerical solution to (6) (solid).

numerical solution well. The asymptotic solutions also show that the boundary layers near the walls have width proportional to $\mathcal{G}^{-1/2}$, consistent with the experimental findings in Sengupta et al. [3]. Fig. 9 plots the director field $\boldsymbol{n}$ and the flow profile u (obtained by using (5)) associated with the equilibria $\theta^*_{a_0,\mathcal{G}}$ and $\theta^*_{a_1,\mathcal{G}}$, computed for $\mathcal{G} = 100$ and $\mathcal{B} = \frac{1}{3}$. The director field is largely flow-aligned, this behavior being typically observed in nematic microfluidics with high flow rates [19]. Furthermore, the director field associated with $\theta^*_{a_0,\mathcal{G}}$ exhibits a third transition layer near the center as predicted by the asymptotic analysis. In contrast to [11], our stability analysis suggests that both solutions are stable when $\mathcal{G} = 100$ and $\mathcal{B} = \frac{1}{3}$.

3.3. Equilibrium solution landscape in $\mathcal{G}$

In this section, we study how the static solution landscape for the system (4) evolves as the pressure gradient $\mathcal{G}$ increases. Figs. 10 and 11 show the evolution of the steady state solutions, $\theta^*_{a_n}$ and $\theta^*_{\bar{a}_n}$, as $\mathcal{G}$ increases. For $\mathcal{G} = 0$ and $\mathcal{B} > \mathcal{B}^*_1$, the trivial solution $\theta^*_{a_0} \equiv 0$ is the unique stable equilibrium. For $\mathcal{G} > 0$ the trivial solution is not an equilibrium and for $\mathcal{B} > \mathcal{B}^*_1$, $\theta^*_{a_0,\mathcal{G}}$ is not the unique stable

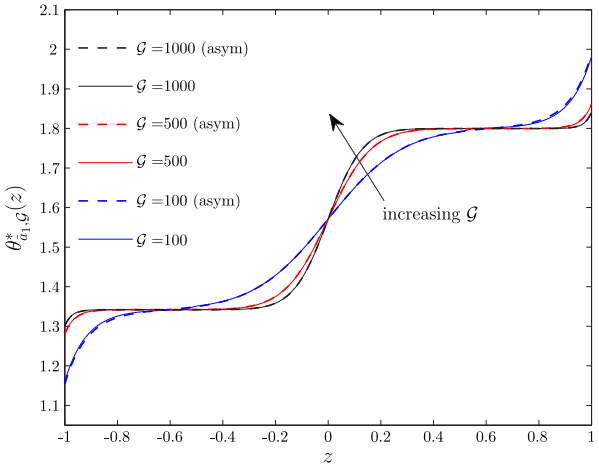

Fig. 8. Static equilibria $\theta^*_{a_1,\mathcal{G}}$ when $\mathcal{G} \to \infty$ and $\mathcal{B} = \frac{1}{3}$. Comparison of asymptotic solution given by (13) (dashed) with the full numerical solution to (6) (solid).

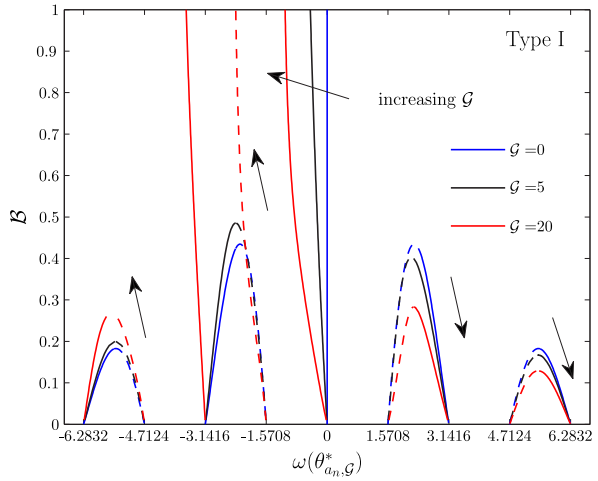

Fig. 10. Evolution of the steady-state solutions of Type I as $\mathcal{G}$ increases. The solid and dashed lines represent, respectively, the values of $\omega(\theta^*_{a_n,\mathcal{G}})$ for which the steady states, $\theta^*_{a_n,\mathcal{G}}$, are stable or unstable.

equilibrium. As the pressure gradient $\mathcal{G}$ increases, new equilibria appear for $\mathcal{B} > \mathcal{B}^*_1$. Additionally, some equilibria, e.g. those with a large positive winding number, become suppressed or have a smaller window of existence in $\mathcal{B}$, as $\mathcal{G}$ increases.

We believe that the asymmetry in the solution branches with positive and negative winding numbers for $\mathcal{G} > 0$ is a consequence of the fact that we work with unit-vector fields, and not director fields without a direction. We speculate that a more sophisticated model, such as the Beris–Edwards model for nematodynamics which accounts for the head–tail symmetry of nematic molecules, may resolve this asymmetry between positive and negative winding numbers for large $\mathcal{G}$.

Let $\mathcal{B}^*_{i,\mathcal{G}}$ denote a critical value of $\mathcal{B}$ for a fixed $\mathcal{G} > 0$; this definition is analogous to the definition of $\mathcal{B}^*_i$ for $\mathcal{G} = 0$. We conjecture that there is a saddle–node bifurcation at each critical value such that if $n > 0$, the stable branch, $\theta^*_{a_{2n},\mathcal{G}}$, and the unstable branch, $\theta^*_{a_{2n-1},\mathcal{G}}$ ($\theta^*_{a_{2n+1},\mathcal{G}}$ for $n < 0$), collide at $\mathcal{B} = \mathcal{B}^*_{2n,\mathcal{G}}$ and cease to exist for $\mathcal{B} > \mathcal{B}^*_{2n,\mathcal{G}}$ (similarly for $\mathcal{B}^*_{2n+1,\mathcal{G}}$ and solutions of Type II). In Fig. 12 we plot the critical values $\mathcal{B}^*_{i,\mathcal{G}} i = \pm 2, 3, \ldots$ as a function of the pressure gradient. For example, if $\mathcal{G} \approx 15$, the critical value $\mathcal{B}^*_{-2,\mathcal{G}} \to \infty$ so that for $\mathcal{G} > 15$, the solution branches $\theta^*_{a_{-2},\mathcal{G}}$ and $\theta^*_{a_{-1},\mathcal{G}}$ do not coalesce and exist for all $\mathcal{B}$.

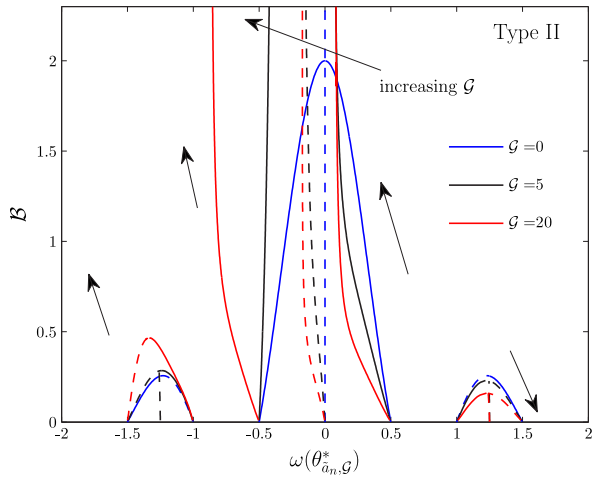

Fig. 11. Evolution of the steady-state solutions of Type II as $\mathcal{G}$ increases. The solid and dashed lines represent, respectively, the values of $\omega(\theta^*_{a_n,\mathcal{G}})$ for which the steady states, $\theta^*_{a_n,\mathcal{G}}$, are stable or unstable.

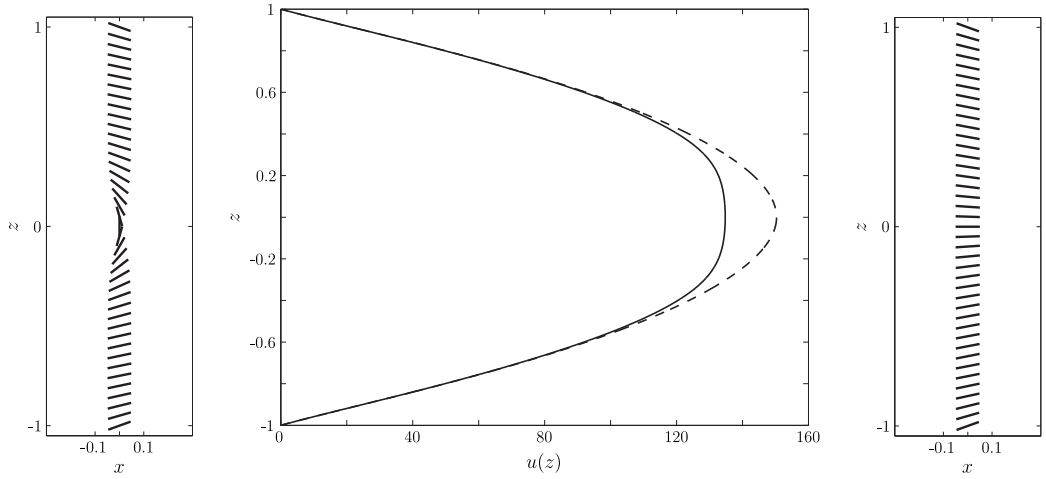

(a) $\boldsymbol{n}$ with $\theta^*_{a_0,100}$. (b) Velocity profiles associated with $\theta^*_{a_0,100}$ (solid) and $\theta^*_{a_1,100}$ (dashed). (c) $\boldsymbol{n}$ with $\theta^*_{a_1,100}$.

Fig. 9. Director and flow profiles associated to the static equilibria $\theta^*_{a_0,100}$ and $\theta^*_{a_1,100}$ when $\mathcal{B} = \frac{1}{3}$.

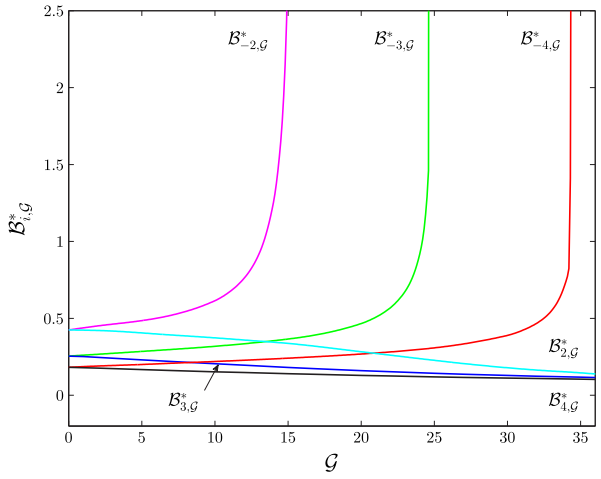

Fig. 12. Evolution of the critical values $\mathcal{B}^*_{i,\mathcal{G}}$ as $\mathcal{G}$ increases.

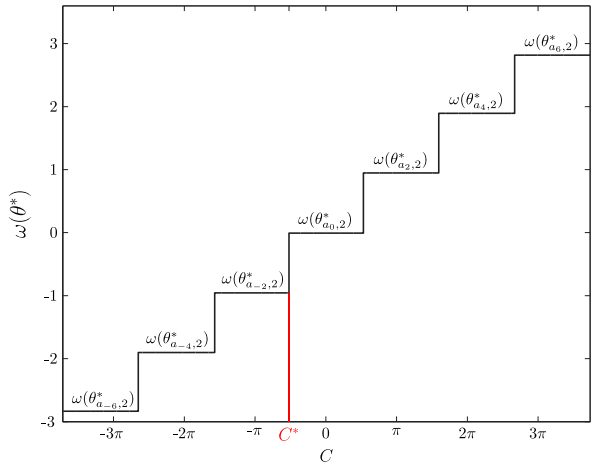

Fig. 13. Winding number for the solution of the system (4) with $\mathcal{B} = \frac{1}{10}$, $\mathcal{G} = 2$, with different linear initial conditions $\Theta(z) = Cz$, $C \in [-7\frac{\pi}{2}, 7\frac{\pi}{2}]$. The critical value C^* is indicated on the x-axis.

4. Time-dependent solutions

In this section, we study the time-dependent behavior of the system (4). We numerically compute the time-dependent solutions using a self-implemented finite-difference method, with mesh resolution $\Delta z = 0.0125$ and time step $\Delta t = 0.01$. As we have seen in Section 3, there are multiple static equilibria for a given pair $(\mathcal{G}, \mathcal{B})$ and it is of interest to investigate steady-state selection, for different choices of the initial conditions. We perform a preliminary investigation of the parameter space by working with either constant or linear initial conditions. We conclude that the time-dependent system converges to:

$$\theta^*_{a_0,\mathcal{G}} \text{ if } \quad \Theta(z) = C, \tag{22}$$

$$\theta^*_{a_n,\mathcal{G}} \text{ if } \quad \Theta(z) = Cz, \tag{23}$$

$$\theta^*_{\tilde{a}_n,\mathcal{G}} \text{ if } \quad \Theta(z) = Cz + \frac{\pi}{2}, \tag{24}$$

where C is a constant. We note that the initial conditions in (22)–(24) do not satisfy the boundary conditions in (4) and in Section 4.1, we propose alternative initial conditions that respect these boundary conditions. In Fig. 13 we use linear initial conditions (23) that have $C \in [-\frac{7\pi}{2}, \frac{7\pi}{2}]$, $\mathcal{G} = 2$, $\mathcal{B} = \frac{1}{10}$, and find that the steady state converges to different equilibria $\theta^*_{a_n,2}$, depending on the initial value C. We compute the corresponding winding numbers and use the winding number to label the static equilibria in Fig. 13. Particularly, for any pair $(\mathcal{G}, \mathcal{B})$, we numerically find a critical value C^* such that if $C \in (C^* - \epsilon, C^* + \epsilon)$, with $\epsilon > 0$ sufficiently small, we have

$$\lim_{t\to\infty} \theta(t, z; Cz) = \begin{cases} \theta^*_{a_{-2},\mathcal{G}} & \text{if } C \in (C^* - \epsilon, C^*), \\ \theta^*_{a_0,\mathcal{G}} & \text{if } C \in [C^*, C^* + \epsilon). \end{cases} \tag{25}$$

Fig. 14 plots the initial condition $\Theta(z) = C^*(z)$, where C^* is the critical value obtained with $\mathcal{G} = 2$ and $\mathcal{B} = \frac{1}{10}$. System (4) with initial condition $\Theta(z) = Cz$ approaches either $\theta^*_{a_0,2}$ or $\theta^*_{a_{-2},2}$ if $C \geq C^*$ or $C < C^*$, respectively.

4.1. Tuning the pressure gradient and the boundary conditions

The pressure gradient and boundary conditions have been assumed to be constants in our computations so far. However, it is of experimental interest to consider situations where both the pressure gradient and boundary conditions are continuously tuned over a short period of time until they attain the desired state. We

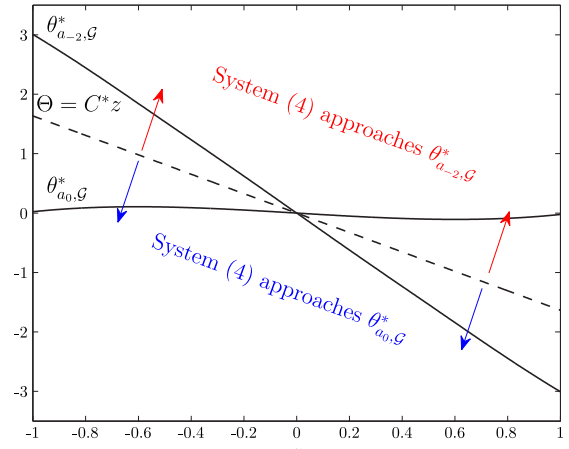

Fig. 14. Solutions $\theta^*_{a_0,\mathcal{G}}$ and $\theta^*_{a_2,\mathcal{G}}$ obtained with $\mathcal{B} = \frac{1}{10}$ and $\mathcal{G} = 2$. The critical initial condition $\Theta(z) = C^* z$ is plotted with dashed line.

consider tuning the flow at a rate δ by applying

$$\mathcal{G}(t) = \begin{cases} 0 & \text{if } t \leq t_1, \\ \bar{\mathcal{G}} \tanh(\delta(t - t_1)) & \text{otherwise.} \end{cases} \tag{26}$$

Similarly, we apply time-dependent anchoring conditions of the form

$$\begin{aligned} &\theta_z(1, t) \\ &= \begin{cases} C & \text{if } t \leq t_2 \\ C(1 - \tanh(\kappa(t - t_2))) \\ \quad - \dfrac{\sin(2\theta(1, t)) \tanh(\kappa(t - t_2))}{\mathcal{B}} & \text{otherwise,} \end{cases} \\ &\theta_z(-1, t) \\ &= \begin{cases} C & \text{if } t \leq t_2 \\ C(1 - \tanh(\kappa(t - t_2))) \\ \quad + \dfrac{\sin(2\theta(1, t)) \tanh(\kappa(t - t_2))}{\mathcal{B}} & \text{otherwise,} \end{cases} \end{aligned} \tag{27}$$

for some constant $\kappa > 0$. In particular, these conditions are satisfied by the initial (linear) condition $\Theta = Cz$ for $t \leq t_2$ and then, the anchoring is switched on with a tuning rate κ, to attain the required weak anchoring conditions at $z = \pm 1$.

We numerically study this modified dynamic system, using (26) and (27), and find that if $t_1 \leq t_2$, then the final steady state is identical to the steady state attained with constant values $\mathcal{G} = \bar{\mathcal{G}}$ and boundary conditions (4c)–(4d), for the parameter sweep

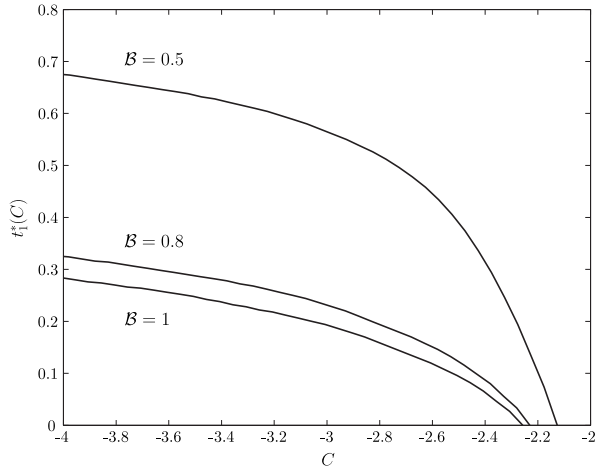

Fig. 15. Critical values $t_1^*(C)$ obtained when solving the system (4), (26)–(27) with $\bar{\mathcal{G}} = 40$, $t_2 = 0$ and $\delta = \kappa = 5$. For $t_1 < t_1^*(C)$, the solution evolves to the steady state $\theta^*_{a_{-2},\bar{\mathcal{G}}}$; for $t_1 \geq t_1^*(C)$, the system evolves to the steady state $\theta^*_{a_0,\bar{\mathcal{G}}}$. Note that $t_1^* = 0$ when $C = C^*$ (see Definition (25)).

that we performed. This indicates that if we first apply a pressure gradient and then enforce strong anchoring, the system will always relax to the same equilibrium state, regardless of the time delay between application of the pressure gradient and anchoring.

On the other hand, if we apply the anchoring condition before the pressure gradient by choosing $t_1 > t_2$, then a different steady state can be attained, depending on the time delay and the respective rates. As an illustrative example, we find that if $\Theta = Cz$ with $C < C^*$ and $\mathcal{B} > \mathcal{B}^*_{-2}$, solutions of system (4) with (26)–(27) may approach the equilibrium solution, $\theta^*_{a_0,\bar{\mathcal{G}}}$, instead of the expected solution, $\theta^*_{a_{-2},\bar{\mathcal{G}}}$. This can be explained as follows: when $t_2 < t \leq t_1$, i.e. while $\mathcal{G} = 0$, the trivial solution $\theta^*_{a_0} = 0$ is the unique steady state and thus the system must approach this solution during the early stages. As a consequence, when the flow begins ($t > t_1$), the solution is already sufficiently close to $\theta^*_{a_0}$ and thus can no longer access the equilibrium state $\theta^*_{a_{-2},\bar{\mathcal{G}}}$, as it would do if $t_1 \leq t_2$. Hence, given model parameters $\bar{\mathcal{G}}$, $\mathcal{B}$, t_2, κ and δ, if the initial condition is $\Theta = Cz$, one can define a critical value $t_1^*(C)$ such that

$$\left\{\begin{array}{ll} \lim_{t\to\infty} \theta(t,z;Cz) = \theta^*_{a_{-2},\bar{\mathcal{G}}} & \text{if } t_1 < t_1^* \\ \lim_{t\to\infty} \theta(t,z;Cz) = \theta^*_{a_0,\bar{\mathcal{G}}} & \text{if } t_1 \geq t_1^*. \end{array}\right\} \tag{28}$$

If C is such that $\lim_{t\to\infty} \theta(t,z;Cz) = \theta^*_{a_{-2},\bar{\mathcal{G}}}$ for all $t_1 > 0$, $t_1^*(C)$ is not defined.

Fig. 15 shows the dependence of the critical times t_1^* on C and $\mathcal{B}$. We observe that, as the inverse anchoring strength $\mathcal{B}$ increases, the critical time $t_1^*(C)$ decreases. This is expected since as $\mathcal{B}$ increases, the anchoring strength decreases and thus the system is able to reorient itself more easily.

5. Conclusions

We have explored the static equilibria of a Leslie–Ericksen model for a unidirectional uniaxial nematic flow in a prototype microfluidic channel, as a function of the pressure gradient $\mathcal{G}$ and inverse anchoring strength, $\mathcal{B}$. As $\mathcal{B} \to 0$, we approach the strong-anchoring limit. Since the Leslie–Ericksen model can be seen as a limiting case of the more general Beris–Edwards and Stark–Lubensky models, we expect that our analytical treatment of the static equilibria may be useful for other researchers in terms of comparison with their flow profile simulations.

We adopt the same model with the same underpinning conditions as in Anderson et al. [11] and build on their work by performing an extensive study of the static solutions (instead of limiting ourselves to two specific steady states). In particular, the weak- and strong-flow solutions (obtained with weak anchoring) in Anderson et al. [11] correspond to $\theta^*_{a_0,\mathcal{G}}$ and $\theta_{\tilde{a}_1,\mathcal{G}}$. As $\mathcal{B} \to 0$, the solution $\theta_{\tilde{a}_1,\mathcal{G}}$ has 1/2-winding number (associated with a rotation by π radians between the top and bottom surfaces) consistent with the Dirichlet conditions for the strong-flow solution in Anderson et al. [11]. Our stability analysis suggests that both solutions are stable when $\mathcal{G} = 0$ and do not lose stability as $\mathcal{G}$ increases. In Anderson et al. [11] the authors report that the strong-flow solution has lower energy than the weak-flow solution for large $\mathcal{G}$ and the critical $\mathcal{G}^*$ depends on the anchoring strength. This is in line with our stability analysis and we speculate that the unstable solution branches in our numerical picture may provide valuable information about how the different solution branches are connected in the full solution landscape. The asymptotic analysis in the limit $\mathcal{G} \to +\infty$ allowed us to obtain useful information about the boundary layers near the center and the channel surfaces, which were experimentally observed by Sengupta et al. [3] in the strong-flow regimes. It is also shown that the transition layer at the center may have a different width compared to the surface boundary layers.

We assume symmetry in the flow profile, which allows the liquid crystal dynamics to be decoupled from the flow dynamics. This enables us to determine explicit and asymptotic solutions that provide key insight into the system behavior. In practice we might expect to observe transitions between the steady states that we have computed here. However, in evolving from one steady state to another the configurations may not exhibit symmetry, and thus this behavior cannot be captured by our model. Solving the fully coupled Leslie–Ericksen model would determine the range of validity of our model in such situations.

We numerically find static equilibria with large winding numbers that are linearly stable within the simple Leslie–Ericksen model. We expect these distorted equilibria to lose stability with respect to perturbations in the x and y directions and so are unlikely to be observable in practice. Finally, we perform a preliminary investigation of the sensitivity of dynamic solutions to initial conditions. Working with a linear initial condition, we numerically find critical values that separate basins of attraction for the distinct steady states. Further, we also study the effect of varying the pressure gradient and anchoring conditions with time and how the rate of change can affect the critical initial conditions that lead to the selection of a particular steady state. This numerical experiment may guide future physical experiments on these lines if experimentalists can control fluid flow and anchoring conditions with time, so as to attain a desired state or at least control transient dynamics. We hope that our results may aid experimentalists to design new control strategies for microfluidic transport and mixing phenomena.

Acknowledgments

This work was carried out thanks to the financial support of the "Spanish Ministry of Economy and Competitiveness" under projects MTM2011-22658 and MTM2015-64865-P. The authors gratefully acknowledge many helpful discussions with L. J. Cummings and D. Vigolo, and discussions at an Oxford Collaborative Workshop Initiative workshop. AM and IMG are grateful for discussions on nematic microfluidics with A. Sengupta. MC thanks the French Labex Numev (grant number APP2016-1-023) (convention ANR-10-LABX-20) for the postdoctoral grant of the First Author at UMR MISTEA, Montpellier, France. AM's research is supported by an EPSRC Career Acceleration Fellowship EP/J001686/1

and EP/J001686/2, an OCIAM Visiting Fellowship and the Advanced Studies Centre at Keble College. IMG gratefully acknowledges support from the Royal Society through a University Research Fellowship.

Appendix A. Leslie–Ericksen continuum theory for nematodynamics

The Leslie–Ericksen dynamic theory is widely accepted to model dynamic phenomena in nematic liquid crystals. A unit vector $\boldsymbol{n} = (n_1, n_2, n_3)$, called the *director*, is defined to describe the local direction of the average molecular alignment in liquid crystals, while the instantaneous motion of the fluid is described by its velocity vector $\boldsymbol{v} = (v_1, v_2, v_3)$. The full equations for nematodynamics describe the evolution of $\boldsymbol{n}$ and $\boldsymbol{v}$. When electromagnetic and gravitational forces are disregarded, the Leslie–Ericksen model for incompressible fluids is [20–23]:

$$v_{i,i} = 0 \qquad \text{in } \Omega, \tag{A.1a}$$

$$\rho \frac{\mathrm{d}v_i}{\mathrm{d}\hat{t}} = \sigma_{ji,j} \qquad \text{in } \Omega \times (0, +\infty), \tag{A.1b}$$

$$\rho_1 \frac{\mathrm{d}}{\mathrm{d}\hat{t}}\Big(\frac{\mathrm{d}n_i}{\mathrm{d}\hat{t}} + \boldsymbol{v}\cdot\nabla n_i\Big) = g_i + \pi_{ji,j} \text{ in } \Omega \times (0, +\infty), \tag{A.1c}$$

where ξ_j denotes the partial derivative of ξ with respect to $\hat{x}_j$ and $\hat{t}$ represents the time. Eqs. (A.1a)–(A.1c) represent mass, linear and angular momentum conservation, respectively, with Ω being the domain occupied by the liquid crystal, ρ is the mass density (assumed constant) and ρ_1 is a constant, measured in terms of weight divided by distance, that arises from the consideration of a rotational kinetic energy of the material element. Here, σ, π and g represent, respectively, the stress tensor, the director stress tensor and the intrinsic director body force. They are defined as

$$\begin{aligned} \sigma_{ji} &= -P\delta_{ij} - \frac{\mathrm{d}F}{\mathrm{d}n_{k,j}} n_{k,i} + \bar{\sigma}_{ji}, \\ \pi_{ji} &= \beta_j n_i + \frac{\mathrm{d}F}{\mathrm{d}n_{i,j}}, \\ g_i &= \gamma n_i - \beta_j n_{i,j} - \frac{\mathrm{d}F}{\mathrm{d}n_i} + \bar{g}_i, \end{aligned} \tag{A.2}$$

where P is the pressure of the fluid flow and δ_{ij} is the Kronecker delta. The vector $(\beta_1, \beta_2, \beta_3)$ and the scalar function γ (sometimes called direction tension) are Lagrange multipliers ensuring $\|\boldsymbol{n}\| = 1$ [23]. F represents the Frank–Oseen free elastic energy, which is associated to distortions of the anisotropic axis. In the case of nematic liquid crystals, F depends on four elastic constants K_i $(i = 1, 2, 3, 4)$, corresponding to the curvature components describing splay, twist, bend and saddle-splay effects (see for instance equation (4.130) in Stewart [24]). Here, we exploit the one-constant approximation of the Frank–Oseen elastic free energy density given by [1]

$$F = \frac{K}{2} n_{i,j} n_{i,j}, \tag{A.3}$$

where K is the only elastic constant considered. This condition has been taken for analytical purposes, since the simpler form of Eq. (A.3) makes it a valuable tool to reach a qualitative insight into distortions in nematics [1]. Note that in this framework, F does not depend on n_i, so that the term $\frac{\mathrm{d}F}{\mathrm{d}n_i}$ appearing in the definition of g_i can be disregarded. Furthermore,

$$\begin{aligned} \bar{\sigma}_{ji} &= \alpha_1 n_k n_p A_{kp} n_i n_j + \alpha_2 N_i n_j \alpha_3 N_j n_i + \alpha_4 A_{ij} \\ &\quad + \alpha_5 A_{ik} n_k n_j + \alpha_6 A_{jk} n_k n_i, \\ N_i &= \frac{\mathrm{d}n_i}{\mathrm{d}\hat{t}} + \boldsymbol{v}\cdot\nabla n_i - \omega_{ij} n_j, \end{aligned}$$

$$\begin{aligned} \omega_{ij} &= \frac{v_{i,j} - v_{j,i}}{2}, \qquad A_{ij} = \frac{v_{i,j} + v_{j,i}}{2}, \quad \text{and} \\ \bar{g}_i &= -\gamma_1 N_i - \gamma_2 n_j A_{ji}, \end{aligned}$$

where α_i are constant viscosities satisfying the Parodi relation [15], $\alpha_2 + \alpha_3 = \alpha_6 - \alpha_5$, and $\gamma_1 = \alpha_3 - \alpha_2$, $\gamma_2 = \alpha_6 - \alpha_5$. More details about these parameters can be found in Appendix A.1.1.

A.1. Simplified model

In this work, we assume that the microfluidic channel, with domain $(0, l) \times (0, w) \times (-h, h)$ has length l much greater than width w and width much greater than height $2h$, so that the director and the flow fields may be assumed to depend only on the $\hat{z}$-coordinate. In the case of the director field, this assumption is not unrealistic for confined systems where the third dimension is very small compared to the lateral dimensions (in our case $l \gg w \gg 2h$) and has been broadly considered in the literature (see e.g. [21,24,25]). In the case of the flow field, this assumption comes from the fact that the flow velocity is dictated by the pressure gradient and, as shown in Anderson et al. [11], is consistent with the experiments in Sengupta et al. [3]. Thus, we let $\boldsymbol{n} = (\sin(\theta(\hat{z}, \hat{t})), 0, \cos(\theta(\hat{z}, \hat{t})))$, $\boldsymbol{v} = (\hat{u}(\hat{z}, \hat{t}), 0, 0)$. Moreover, $\hat{u}(\hat{z}, \hat{t})$ is considered symmetric around $\hat{z} = 0$ and the no-slip condition is assumed in the channel walls (i.e. $\hat{u}(\pm h, \hat{t}) = 0$).

Using this information in the constitutive formulas, one has that

- $A_{ij} = 0$ except for $A_{13} = A_{31} = \frac{\hat{u}_{\hat{z}}}{2}$.
- $\omega_{ij} = 0$ except for $\omega_{13} = \frac{\hat{u}_{\hat{z}}}{2}$ and $\omega_{31} = \frac{-\hat{u}_{\hat{z}}}{2}$.
- $N_1 = n_{1,\hat{t}} - w_{13} n_3 = \cos(\theta)\theta_{\hat{t}} - \frac{\hat{u}_{\hat{z}}}{2}\cos(\theta) = \cos(\theta)(\theta_{\hat{t}} - \frac{hatu_{\hat{z}}}{2})$.
- $N_2 = 0$.
- $N_3 = n_{3,\hat{t}} - w_{31} n_1 = -\sin(\theta)\theta_{\hat{t}} + \frac{\hat{u}_{\hat{z}}}{2}\sin(\theta) = \sin(\theta)(\frac{\hat{u}_{\hat{z}}}{2} - \theta_{\hat{t}})$.
- $\bar{g}_1 = -\gamma_1 N_1 - \gamma_2 A_{31} n_3 = \frac{\cos(\theta)\hat{u}_{\hat{z}}}{2}(\gamma_1 - \gamma_2) - \gamma_1 \cos(\theta)\theta_{\hat{t}}$.
- $\bar{g}_2 = 0$.
- $\bar{g}_3 = -\gamma_1 N_3 - \gamma_2 A_{13} n_1 = -\frac{\sin(\theta)\hat{u}_{\hat{z}}}{2}(\gamma_1 + \gamma_2) + \gamma_1 \sin(\theta)\theta_{\hat{t}}$.

Now, taking into account that F only depends on the variables $n_{1,3}$ and $n_{3,3}$ one has that $\pi_{ij,i} = 0$ except for $\pi_{31,3}$ and $\pi_{33,3}$. Thus,

- $\pi_{31,3} = \left(\frac{\mathrm{d}F}{\mathrm{d}n_{1,3}}\right)_{,3} = Kn_{1,33}$.
- $\pi_{33,3} = \left(\frac{\mathrm{d}F}{\mathrm{d}n_{3,3}}\right)_{,3} = Kn_{3,33}$.
- $g_1 = \gamma n_1 + \bar{g}_1 = \gamma n_1 + \frac{\cos(\theta)\hat{u}_{\hat{z}}}{2}(\gamma_1 - \gamma_2) - \gamma_1 \cos(\theta)\theta_{\hat{t}}$.
- $g_2 = 0$.
- $g_3 = \gamma n_3 + \bar{g}_3 = \gamma n_3 - \frac{\sin(\theta)\hat{u}_{\hat{z}}}{2}(\gamma_1 + \gamma_2) + \gamma_1 \sin(\theta)\theta_{\hat{t}}$.
- $\bar{\sigma}_{ij} = 0$ except for $\bar{\sigma}_{11}$, $\bar{\sigma}_{13}$, $\bar{\sigma}_{31}$ and $\bar{\sigma}_{33}$.

In our case, it follows from the linear momentum equation (A.1b) that

$$\begin{aligned} \rho\frac{\mathrm{d}\hat{u}}{\mathrm{d}\hat{t}} &= \sigma_{11,1} + \sigma_{31,3} = -P_{,1} + \bar{\sigma}_{31,3}, \\ 0 &= \sigma_{22,2} = -P_{,2}, \\ 0 &= \sigma_{33,3} = -(P + 2F)_{,3} + \bar{\sigma}_{33,3}. \end{aligned}$$

Note that we will use the notation $f_{,1}, f_{,2}, f_{,3}$; $f_{,\hat{x}}, f_{,\hat{y}}, f_{,\hat{z}}$ and $f_{\hat{x}}, f_{\hat{y}}, f_{\hat{z}}$ interchangeably. Therefore, it follows from (A.1b) that

$$-(P + 2F)_{\hat{x}} + \bar{\sigma}_{31,\hat{z}} = \rho\frac{\mathrm{d}\hat{u}}{\mathrm{d}\hat{t}} \text{ in } (0, l) \times (0, w) \times (-h, h) \times (0, +\infty), \tag{A.4a}$$

$$(P + 2F)_{\hat{y}} = 0 \qquad \text{in } (0, l) \times (0, w) \times (-h, h) \times (0, +\infty), \tag{A.4b}$$

$$-(P + 2F)_{\hat{z}} + \bar{\sigma}_{33,\hat{z}} = 0 \qquad \text{in } (0, l) \times (0, w) \times (-h, h) \times (0, +\infty). \tag{A.4c}$$

The Reynolds number for the flow can be defined as $Re = \rho U l/\alpha_4$, where l is a representative axial length of the channel and U is a typical axial velocity. Since $U = l/\tau$, where $\tau = K/\alpha_4 h^2$ is the relevant timescale of interest in the channel (see Eq. (3)), this gives a reduced Reynolds number $\epsilon^2 Re \equiv (h/l)^2 Re = \rho K/\alpha_4^2 \ll 1$.[3,11] Thus we may safely neglect the inertial terms, i.e., $\rho \mathrm{d}\hat{u}/\mathrm{d}\hat{t} = 0$ in Eq. (A.4a). From (A.4b), one has that $P + 2F = q(\hat{x}, \hat{z}, \hat{t})$. Now, if we integrate with respect to $\hat{x}$ in Eq. (A.4a) and take into account that F only depends on $\hat{z}$ and $\hat{t}$,

$$P + 2F = \hat{x}\bar{\sigma}_{31,\hat{z}} + r(\hat{z}, \hat{t}). \tag{A.5}$$

If relation (A.5) is introduced in Eq. (A.4c), one has that $(\hat{x}\bar{\sigma}_{31,\hat{z}} + r(\hat{z}, \hat{t}))_{,\hat{z}} = \bar{\sigma}_{33,\hat{z}}$. Consequently, $\bar{\sigma}_{31,\hat{z}\hat{z}} = 0$, and so

$$\bar{\sigma}_{31} = C(\hat{t})\hat{z} + D(\hat{t}), \tag{A.6}$$

where $C(\hat{t})$ and $D(\hat{t})$ are functions to be determined. Then, from relation (A.5), one has that

$$P + 2F = C(\hat{t})\hat{x} + r(\hat{z}, \hat{t}). \tag{A.7}$$

From Eqs. (A.7) and (A.4c) it follows that $(C(\hat{t})\hat{x} + r(\hat{z}, \hat{t}))_{,\hat{z}} = (r(\hat{z}, \hat{t}))_{,\hat{z}} = \bar{\sigma}_{33,\hat{z}}$, where integrating with respect to $\hat{z}$ one has that $r(\hat{z}, \hat{t}) = \bar{\sigma}_{33} + s(\hat{t})$, s being a time-dependent function to be determined. Returning to Eq. (A.7), it follows that

$$P = -2F + C(\hat{t})\hat{x} + s(\hat{t}) + \bar{\sigma}_{33}. \tag{A.8}$$

Replacing the value of $\bar{\sigma}_{31}$ in Eq. (A.6) one has that

$$\hat{u}_{\hat{z}} g(\theta) + \theta_{\hat{t}} m(\theta) = C(\hat{t})\hat{z} + D(\hat{t}).$$

A consequence of the symmetry of $\hat{u}$ enforces $\frac{\partial \theta}{\partial \hat{t}} = 0$ at $\hat{z} = 0$. Any scenario for which $\frac{\partial \theta}{\partial \hat{t}} \neq 0$ would induce a velocity profile that is non-symmetric and thus violate our original assumption. As a result, this implies that $D(\hat{t}) = 0$ for our system and hence

$$\hat{u}_{\hat{z}} g(\theta) + \theta_{\hat{t}} m(\theta) = C(\hat{t})\hat{z}, \tag{A.9}$$

where

$$g(\theta) = \alpha_1 \cos^2(\theta)\sin^2(\theta) + \frac{\alpha_5 - \alpha_2}{2}\cos^2(\theta) + \frac{\alpha_3 + \alpha_6}{2}\sin^2(\theta) + \frac{\alpha_4}{2}, \tag{A.10a}$$

$$m(\theta) = \alpha_2 \cos^2(\theta) - \alpha_3 \sin^2(\theta). \tag{A.10b}$$

Note that we have reduced Eqs. (A.4a)–(A.4c) to Eq. (A.9), the pressure being available via Eq. (A.8). Now, the angular momentum balance Eq. (A.1c) for $i = 1$ and $i = 3$ reduces, respectively, to

$$\begin{aligned}\rho_1 n_{1,\hat{t}\hat{t}} &= g_1 + \pi_{31,3} = \gamma n_1 + \bar{g}_1 \\ &\quad + \pi_{31,3} = \gamma n_1 + \bar{g}_1 + K n_{1,33}, \\ \rho_1 n_{3,\hat{t}\hat{t}} &= g_3 + \pi_{33,3} = \gamma n_3 + \bar{g}_3 \\ &\quad + \pi_{33,3} = \gamma n_3 + \bar{g}_3 + K n_{3,33}.\end{aligned}$$

It remains to compute $n_{1,33}$, $n_{3,33}$, $n_{1,\hat{t}\hat{t}}$ and $n_{2,\hat{t}\hat{t}}$:

- $n_1 = \sin(\theta) \Rightarrow n_{1,3} = \cos(\theta)\theta_{\hat{z}} \Rightarrow n_{1,33} = -\sin(\theta)(\theta_{\hat{z}})^2 + \cos(\theta)\theta_{\hat{z}\hat{z}}$,
- $n_{1,\hat{t}} = \cos(\theta)\theta_{\hat{t}} \Rightarrow n_{1,\hat{t}\hat{t}} = -\sin(\theta)(\theta_{\hat{t}})^2 + \cos(\theta)\theta_{\hat{t}\hat{t}}$,
- $n_3 = \cos(\theta) \Rightarrow n_{3,3} = -\sin(\theta)\theta_{\hat{z}} \Rightarrow n_{3,33} = -\cos(\theta)(\theta_{\hat{z}})^2 - \sin(\theta)\theta_{\hat{z}\hat{z}}$,
- $n_{3,\hat{t}} = -\sin(\theta)\theta_{\hat{t}} \Rightarrow n_{3,\hat{t}\hat{t}} = -\cos(\theta)(\theta_{\hat{t}})^2 - \sin(\theta)\theta_{\hat{t}\hat{t}}$.

Thus, Eq. (A.1c) when $i = 1$ and $i = 3$ becomes

$$\begin{aligned}&\rho_1(-\sin(\theta)(\theta_{\hat{t}})^2 + \cos(\theta)\theta_{\hat{t}\hat{t}}) \\ &\quad = \gamma \sin(\theta) - \gamma_1 \cos(\theta)\theta_{\hat{t}} + \cos(\theta)\frac{\hat{u}_{\hat{z}}}{2}(\gamma_1 - \gamma_2) \\ &\qquad + K(-\sin(\theta)\theta_{\hat{z}}^2 + \cos(\theta)\theta_{\hat{z}\hat{z}}), \\ &\rho_1(-\cos(\theta)(\theta_{\hat{t}})^2 - \sin(\theta)\theta_{\hat{t}\hat{t}}) \\ &\quad = \gamma \cos(\theta) + \gamma_1 \sin(\theta)\theta_{\hat{t}} - \sin(\theta)\frac{\hat{u}_{\hat{z}}}{2}(\gamma_1 + \gamma_2) \\ &\qquad + K(-\cos(\theta)\theta_{\hat{z}}^2 - \sin(\theta)\theta_{\hat{z}\hat{z}}).\end{aligned}$$

We neglect the term $\rho_1 \theta_{\hat{t}\hat{t}}$, since the rotational inertia of the molecules is accepted to be much smaller than the elastic and viscous torques [25]. Then, multiplying the first equation by $\cos(\theta)$, the second one by $\sin(\theta)$ and subtracting them, one obtains:

$$\gamma_1 \theta_{\hat{t}} = K\theta_{\hat{z}\hat{z}} + \frac{\hat{u}_{\hat{z}}}{2}\big(\gamma_1 - \gamma_2 \cos(2\theta)\big). \tag{A.11}$$

Thus, the evolution of θ and $\hat{u}$ are described by the following system

$$\gamma_1 \theta_{\hat{t}} = K\theta_{\hat{z}\hat{z}} - \hat{u}_{\hat{z}} m(\theta) \qquad \hat{z} \in (-h, h), \hat{t} > 0, \tag{A.12a}$$

$$C(\hat{t})\hat{z} = \hat{u}_{\hat{z}} g(\theta) + \theta_{\hat{t}} m(\theta) \qquad \hat{z} \in (-h, h), \hat{t} > 0, \tag{A.12b}$$

$$\theta(\hat{z}, 0) = \Theta(\hat{z}) \qquad \hat{z} \in (-h, h), \tag{A.12c}$$

$$\hat{u}(\pm h, \hat{t}) = 0 \qquad \hat{t} > 0, \tag{A.12d}$$

where Θ is the initial condition for θ and $C(\hat{t}) = P_{\hat{x}}$, i.e., the channel direction component of the pressure gradient. Although system (A.12) has been derived from the Leslie–Ericksen model (A.1), it can be also obtained by simplifying the more general Beris–Edwards and Stark–Lubensky models [10,26,27].

A.1.1. Remarks on coefficients

The coefficients α_i and γ_i are usually called *Leslie Coefficients* (see for instance Lee [28] or Wang et al. [25] for further information about their physical meaning and how to approximate them experimentally). They depend only on the temperature and have the dimension of viscosity. Some constraints on the *Leslie Coefficients* come from the non-negativity of the *Dissipative function*, [21,24]. When the Parodi relation is used [15], the dissipative function is defined as [24]:

$$\begin{aligned}\mathcal{D} &= \alpha_1(n_i A_{ij} n_j)^2 + 2\gamma_2 N_i A_{ij} n_j \\ &\quad + \alpha_4 A_{ij} A_{ij} + (\alpha_5 + \alpha_6) A_{ij} A_{jk} n_i n_k + \gamma_1 N_i N_i.\end{aligned}$$

In our particular case,

$$\begin{aligned}\mathcal{D} &= \alpha_1 \hat{u}_{\hat{z}}^2 \sin^2(\theta)\cos^2(\theta) \\ &\quad + 2\gamma_2 \frac{\hat{u}_{\hat{z}}}{2}\left(\theta_{\hat{t}} - \frac{\hat{u}_{\hat{z}}}{2}\right)(\cos^2(\theta) - \sin^2(\theta)) \\ &\quad + \alpha_4 \frac{\hat{u}_{\hat{z}}^2}{2} + (\alpha_5 + \alpha_6)\frac{\hat{u}_{\hat{z}}^2}{4} + \gamma_1\left(\theta_{\hat{t}} - \frac{\hat{u}_{\hat{z}}}{2}\right)^2 \\ &= 2\theta_{\hat{t}}\hat{u}_{\hat{z}} m(\theta) + \gamma_1 \theta_{\hat{t}}^2 + g(\theta)\hat{u}_{\hat{z}}^2.\end{aligned}$$

This expression is a quadratic form and can be rewritten as:

$$\mathcal{D} = \begin{bmatrix} X & Y \end{bmatrix} \begin{bmatrix} g(\theta) & m(\theta) \\ m(\theta) & \gamma_1 \end{bmatrix} \begin{bmatrix} X \\ Y \end{bmatrix},$$

with $X = \hat{u}_{\hat{z}}$, $Y = \theta_{\hat{t}}$.

A reasonable assumption is that the dissipation function is positive [24], which is fulfilled if and only if the determinant of every principal submatrix is positive [29], i.e.,

$$g(\theta) > 0 \quad \text{and} \quad \gamma_1 g(\theta) - m^2(\theta) > 0. \tag{A.13}$$

When $\theta = 0$, this implies that

$$\gamma_1 > 0, \qquad \alpha_5 - \alpha_2 + \alpha_4 > 0 \quad \text{and} \quad \gamma_1(\alpha_5 - \alpha_2 + \alpha_4) > 2\alpha_2^2.$$

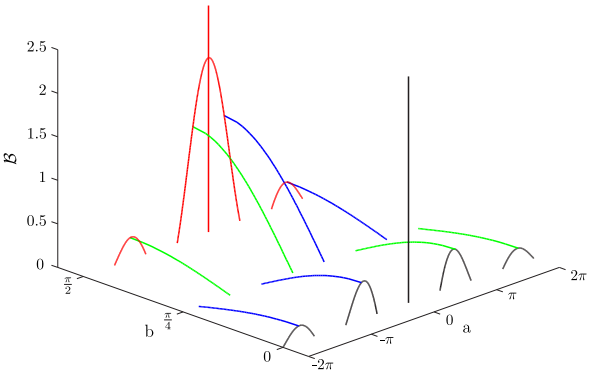

Fig. B.16. Solution landscape with $a \in [-2\pi, 2\pi]$ and $b \in [0, \frac{\pi}{2}]$. Solutions of Type I (Type II) correspond to $b = 0$ ($b = \frac{\pi}{2}$) and are plotted in black (red). Solutions of Types III and IV correspond to $b \in [0, \frac{\pi}{2}]$ and are plotted in blue and green, respectively. (For interpretation of the references to color in this figure legend, the reader is referred to the web version of this article.)

Appendix B. Equilibrium Solutions with $\mathcal{G} = 0$

When $\mathcal{G} = 0$, we can explicitly solve the first equation of system (6) to obtain $\theta^*(z) = az + b$ where a and b are constants to be determined by the boundary conditions. These solutions may be categorized as

$$\text{Type I } \theta^*(z) = a_n z + m\pi, \qquad \text{where } m \in \mathbb{Z} \text{ and } \mathcal{B}a_n = -\sin(2a_n), \quad \text{(B.1)}$$

$$\text{Type II } \theta^*(z) = \tilde{a}_n z + \left(m + \frac{1}{2}\right)\pi, \qquad \text{where } m \in \mathbb{Z} \text{ and } \mathcal{B}\tilde{a}_n = \sin(2\tilde{a}_n), \quad \text{(B.2)}$$

$$\text{Type III } \theta^*(z) = \left(n + \frac{1}{4}\right)\pi z + b_m, \qquad \text{where } n \in \mathbb{Z} \text{ and } \cos(2b_m) = -\mathcal{B}\left(n + \frac{1}{4}\right)\pi, \quad \text{(B.3)}$$

$$\text{Type IV } \theta^*(z) = \left(n + \frac{3}{4}\right)\pi z + \tilde{b}_m, \qquad \text{where } n \in \mathbb{Z} \text{ and } \cos(2\tilde{b}_m) = \mathcal{B}\left(n + \frac{3}{4}\right)\pi. \quad \text{(B.4)}$$

For every value of $\mathcal{B}$, we obtain ordered set of solutions for (B.1), with $0 = a_0 < a_1 < \cdots < a_n$ ($n \in \mathbb{N} \cup \{0\}$ depending on $\mathcal{B}$). Furthermore, if a_n provides a solution, so does $-a_n$, which we denote by a_{-n}. Equivalent statement can be made for $\tilde{a}_n$, b_m and $\tilde{b}_m$, solutions of equations (B.2), (B.3) and (B.4), respectively.

We observe that constant solutions of Types I and II, $\theta^* \equiv k\frac{\pi}{2}$ ($k \in \mathbb{Z}$) exist for all values of $\mathcal{B}$, while solutions of Types III and IV exist only if $\mathcal{B} \leq \frac{4}{\pi}$. The associated director fields are

$$\begin{aligned}
&\text{Type I} \quad \boldsymbol{n}(z) = (-1)^m(\sin(a_n z), 0, \cos(a_n z)),\\
&\text{Type II} \quad \boldsymbol{n}(z) = (-1)^m(\cos(\tilde{a}_n z), 0, -\sin(\tilde{a}_n z)),\\
&\text{Type III} \quad \boldsymbol{n}(z) = (-1)^m\left(\sin\left(\left(n + \frac{1}{4}\right)\pi z + b_0\right), 0, \cos\left(\left(n + \frac{1}{4}\right)\pi z + b_0\right)\right)\\
&\text{Type IV} \quad \boldsymbol{n}(z) = (-1)^m\left(\sin\left(\left(n + \frac{3}{4}\right)\pi z + \tilde{b}_0\right), 0, \cos\left(\left(n + \frac{3}{4}\right)\pi z + \tilde{b}_0\right)\right)
\end{aligned}$$

and thus, since director fields with $m \in \mathbb{Z}$ are the same but with opposite direction, all possible director profiles in (B.1)–(B.4) are covered by $m = 0$. Fig. B.16 shows the solution landscape in terms of a, b and $\mathcal{B}$, restricted to $a \in [2\pi, 2\pi]$ and $b \in [0, \frac{\pi}{2}]$.

Since solutions of Types III and IV are always unstable (see Appendix B.1), we only track solutions of Types I and II in this paper.

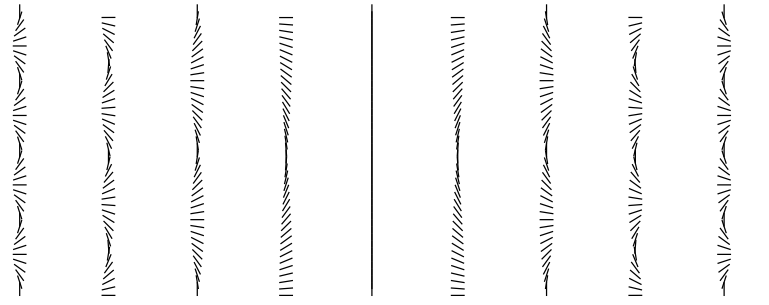

Fig. B.17. $\boldsymbol{n}$ associated with steady states $\theta^*_{a_n}$ (Type I), obtained with $\mathcal{B} = 0.001$ and $\mathcal{G} = 0$. These states are stable if n is even and unstable if n is odd.

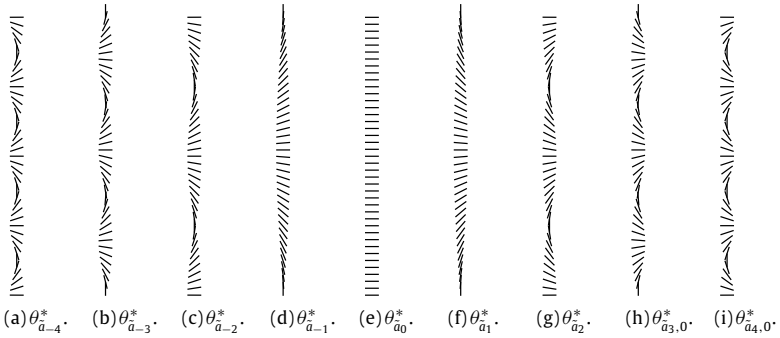

Fig. B.18. $\boldsymbol{n}$ associated with steady states $\theta^*_{\tilde{a}_n}$ (Type II), obtained with $\mathcal{B} = 0.001$ and $\mathcal{G} = 0$. These states are stable if n is odd and unstable if n is even.

B.1. Linear Stability of Equilibrium Solutions

B.1.1. Sample liquid crystal molecular configurations

In this section we show the director field corresponding to some steady state solutions of the system (4) with $\mathcal{G} = 0$. Particularly, Figs. B.17 and B.18 show the director profiles associated, respectively, to solutions $\theta^*_{a_n}$ and $\theta^*_{\tilde{a}_n}$, $n = 0, \pm1, \pm2 \pm 3, \pm4$.

References

[1] P.G. de Gennes, J. Prost, The Physics of Liquid Crystals, in: International Series of Monographs on Physics, Clarendon Press, 1993.
[2] A. Sengupta, Topological Microfluidics: Nematic Liquid Crystals and Nematic Colloids in Microfluidic Environment (Springer Theses), Springer International Publishing, 2013.
[3] A. Sengupta, U. Tkalec, M. Ravnik, J.M. Yeomans, C. Bahr, S. Herminghaus, Liquid crystal microfluidics for tunable flow shaping, Phys. Rev. Lett. 110 (4) (2013) 048303.
[4] T.J. Sluckin, D.A. Dunmur, H. Stegemeyer, Crystals That Flow: Classic Papers from the History of Liquid Crystals, in: Liquid Crystals Book Series, Taylor & Francis, 2004.
[5] F.M. Leslie, Continuum theory for nematic liquid crystals, Contin. Mech. Thermodyn. 4 (3) (1992) 167–175.
[6] O.D. Lavrentovich, Transport of particles in liquid crystals, Soft Matter 10 (2014) 1264–1283.
[7] H.A. Stone, A.D. Stroock, A. Ajdari, Engineering flows in small devices: microfluidics toward a lab-on-a-chip, Annu. Rev. Fluid Mech. 36 (2004) 381–411.
[8] G.M. Whitesides, The origins and the future of microfluidics, Nature 442 (7101) (2006) 368–373.
[9] Y.K. Kim, B. Senyuk, O.D. Lavrentovich, Molecular reorientation of a nematic liquid crystal by thermal expansion, Nature Commun. 3 (2012) 1133.
[10] C. Denniston, E. Orlandini, J.M. Yeomans, Lattice Boltzmann simulations of liquid crystal hydrodynamics, Phys. Rev. E 63 (2001) 056702.
[11] T.G. Anderson, E. Mema, L. Kondic, L.J. Cummings, Transitions in Poiseuille flow of nematic liquid crystal, Int. J. Non-Linear Mech. 75 (2015) 15–21.
[12] V.M.O. Batista, M.L. Blow, M.M. Telo da Gama, The effect of anchoring on the nematic flow in channels, Soft Matter 11 (2015) 4674–4685.
[13] G. Bevilacqua, G. Napoli, Parity of the weak Fréedericksz transition, Eur. Phys. J. E 35 (12) (2012) 1–5.
[14] A. Rapini, M. Papoular, Distorsion d'une lamelle nématique sous champ magnétique conditions d'ancrage aux parois, J. Phys. Colloq. 30 (C4) (1969) C4–54, C4–56.
[15] O. Parodi, Stress tensor for a nematic liquid crystal, J. Phys. France 31 (7) (1970) 581–584.
[16] N.D. Mermin, The topological theory of defects in ordered media, Rev. Modern Phys. 51 (1979) 591–648.
[17] E.L. Allgower, K. Georg, Introduction to Numerical Continuation Methods, in: Classics in Applied Mathematics, Society for Industrial and Applied Mathematics, 2003.
[18] S.A. Jewell, S.L. Cornford, F. Yang, P.S. Cann, J.R. Sambles, Flow-driven transition and associated velocity profiles in a nematic liquid-crystal cell, Phys. Rev. E 80 (2009) 041706.
[19] A. Rey, M.M. Denn, Converging flow of tumbling nematic liquid crystals, Liq. Cryst. 4 (3) (1989) 253–272.
[20] F.M. Leslie, Theory of flow phenomena in liquid crystals, Adv. Liq. Cryst. 4 (4) (1979) 1–81.
[21] F.M. Leslie, Some constitutive equations for liquid crystals, Arch. Ration. Mech. Anal. 28 (4) (1968) 265–283.
[22] J.L. Ericksen, Anisotropic fluids, Arch. Ration. Mech. Anal. 4 (1) (1959) 231.
[23] H. Wu, X. Xu, C. Liu, On the general Leslie–Ericksen system: Parodi's relation, well-posedness and stability, Arch. Ration. Mech. Anal. 208 (2013) 59–107.
[24] I.W. Stewart, The Static and Dynamic Continuum Theory of Liquid Crystals: A Mathematical Introduction, in: Liquid Crystals Book Series, Taylor & Francis, 2004.
[25] H. Wang, T.X. Wu, S. Gauza, J.R. Wu, S. Wu, A method to estimate the Leslie coefficients of liquid crystals based on MBBA data, Liq. Cryst. 33 (1) (2006) 91–98.
[26] T. Qian, P. Sheng, Generalized hydrodynamic equations for nematic liquid crystals, Phys. Rev. E 58 (1998) 7485.
[27] H. Stark, T.C. Lubensky, Poisson-bracket approach to the dynamics of nematic liquid crystals, Phys. Rev. E 67 (2003) 061709.
[28] S. Lee, The Leslie coefficients for a polymer nematic liquid crystal, J. Chem. Phys. 88 (8) (1988) 5196–5201.
[29] J.A. Infante, J.M. Rey, Métodos Numéricos, Teoría, Problemas y Prácticas Con MATLAB, Ediciones Pirámide, Grupo Anaya, 2015.